# King's Research Portal

[Link to publication record in King's Research Portal](#)

1    **Iron derived from autophagy-mediated ferritin degradation induces cardiomyocyte**

2    **death and heart failure in mice**

3

4    Jumpei Ito[1,2], Shigemiki Omiya[1], Mara-Camelia Rusu[1], Hiromichi Ueda[3], Tomokazu

5    Murakawa[1], Yohei Tanada[1], Hajime Abe[1], Kazuki Nakahara[1], Michio Asahi[2], Manabu

6    Taneike[1,3], Kazuhiko Nishida[1], Ajay M. Shah[1], Kinya Otsu[1,*]

7

8    [1]The School of Cardiovascular Medicine and Sciences, King's College London British Heart

9    Foundation Centre of Excellence, 125 Coldharbour Lane, London SE5 9NU, United Kingdom.

10   [2]Department of Pharmacology, Faculty of Medicine, Osaka Medical College, 2-7

11   Daigakumachi, Takatsuki, Osaka 569-8686, Japan. [3]Department of Cardiovascular Medicine,

12   Graduate School of Medicine, Osaka University, 2-2 Yamadaoka, Suita, Osaka 565-0871,

13   Japan.

14

15   *Address for Correspondence:

16   Kinya Otsu

17   The School of Cardiovascular Medicine and Sciences, King's College London British Heart

18   Foundation Centre of Excellence, 125 Coldharbour Lane, London SE5 9NU, United Kingdom.

19   Tel: +44-020-7848-5128, Email address: kinya.otsu@kcl.ac.uk

20   **Abstract**

21   Heart failure is a major public health problem, and abnormal iron metabolism is common in

22   patients with heart failure. Although iron is necessary for metabolic homeostasis, it induces a

23   programmed necrosis. Iron release from ferritin storage is through nuclear receptor coactivator

24   4 (NCOA4)-mediated autophagic degradation, known as ferritinophagy. However, the role of

25   ferritinophagy in the stressed heart remains unclear. Deletion of *Ncoa4* in mouse hearts reduced

26   left ventricular chamber size and improved cardiac function along with the attenuation of the

27   upregulation of ferritinophagy-mediated ferritin degradation four weeks after pressure

28   overload. Free ferrous iron overload and increased lipid peroxidation were suppressed in

29   NCOA4-deficient hearts. A potent inhibitor of lipid peroxidation, ferrostatin-1, significantly

30   mitigated the development of pressure overload-induced dilated cardiomyopathy in wild-type

31   mice. Thus, the activation of ferritinophagy results in the development of heart failure, whereas

32   inhibition of this process protects the heart against hemodynamic stress.

**Introduction**

Heart failure is the leading cause of death in developed countries (Ponikowski et al., 2016). There is substantial evidence to suggest the involvement of oxidative stress and cardiomyocyte death in the pathogenesis of heart failure (Whelan et al., 2010). Iron metabolism in heart failure patients is dysregulated (Lavoie, 2020), but it remains unclear whether these changes are pathogenetic and detrimental or adaptative and protective for the heart. While iron is essential for oxidative phosphorylation, metabolite synthesis, and oxygen transport (Andrews et al., 2007), it can generate toxic reactive hydroxyl radicals through the Fenton reaction (Papanikolaou et al., 2005). Iron-dependent necrotic cell death is characterized by iron overload and an increased level of lipid reactive oxygen species (ROS) such as lipid hydroperoxides, leading to phospholipid damage, plasma membrane disruption, and caspase- and necrosome-independent cell death (Dixon et al., 2012). Ferroptosis is a form of iron-dependent necrosis. Multiple molecular components contribute to the execution of ferroptosis, such as transferrin–iron, cystine–glutathione, and glutamine pathways (Gao et al., 2015). Glutathione peroxidase 4 (GPX4) is a phospholipid hydroperoxide-reducing enzyme that uses glutathione as a substrate. The failure of GPX4 to clear lipid ROS leads to lipid peroxidation and ferroptosis (Yang et al., 2014). Glutamate through the glutamine-fueled intracellular metabolic process glutaminolysis induces ferroptosis (Gao et al., 2015). Ferroptosis has been implicated in the pathological process associated with ROS-induced tissue injury, such as ischemia/reperfusion in the brain, kidney, and heart (Fang et al., 2019; Linkermann et al., 2014; Tuo et al., 2017).

Iron is stored in ferritin protein complexes in the cell to prevent an increase in the size of the labile iron pool that normally follows iron overload. Ferritin is a ubiquitously expressed cytosolic heteropolymer composed of H-chains (FTH1) and L-chains (FTL) (Arosio et al., 2009). FTH1 has ferroxidase activity and sequestrates ferrous iron ($Fe^{2+}$) from the Fenton reaction in which the spontaneous oxidation to ferric iron ($Fe^{3+}$) donates single electrons to

transform innocuous hydrogen peroxide to highly toxic hydroxyl free radicals. In the case of iron overload, ferritin subunits are induced by inactivating the iron regulatory protein (IREB)/iron-responsive element pathway. By contrast, under conditions of iron deficiency or increased iron requirement, ferritin is degraded, mediated through a selective form of autophagy, called ferritinophagy. Nuclear receptor coactivator 4 (NCOA4) is a cargo receptor for ferritinophagy, that interacts with FTH1 and promotes the transport of ferritin to the autophagosome for degradation (Dowdle et al., 2014; Mancias et al., 2014). NCOA4-dependent iron release from ferritin storage is necessary for erythropoiesis (Bellelli et al., 2016).

67 **Results**

68

69 **Generation and characterization of cardiomyocyte-specific NCOA4-deficient mice**

70 To examine the *in vivo* role of NCOA4-dependent ferritin degradation in the heart,

71 cardiomyocyte-specific NCOA4-deficient mice were generated (Figure 1—figure supplement

72 1A and B). The homozygous floxed *Ncoa4* mice (*Ncoa4*<sup>flox/flox</sup>) appeared normal and were

73 externally indistinguishable from littermates of other genotypes. The *Ncoa4*<sup>flox/flox</sup> mice were

74 crossed with transgenic mice expressing α-myosin heavy chain (*Myh6*) promoter-driven Cre

75 recombinase (Myh6-Cre) (Nishida et al., 2004) to generate cardiomyocyte-specific NCOA4-

76 deficient mice (*Ncoa4*<sup>−/−</sup>), *Ncoa4*<sup>flox/flox</sup>;Myh6-Cre<sup>+</sup>. The *Ncoa4*<sup>flox/flox</sup>;Myh6-Cre<sup>−</sup> littermates

77 were used as controls (*Ncoa4*<sup>+/+</sup>). The *Ncoa4*<sup>+/+</sup> and *Ncoa4*<sup>−/−</sup> mice were born at the expected

78 Mendelian ratio (54 and 51 mice, respectively), and they grew to adulthood and were fertile.

79 The protein and mRNA levels of NCOA4 were significantly decreased in *Ncoa4*<sup>−/−</sup> hearts by

80 84% and 81% compared to control, respectively (Figure 1—figure supplement 1C and D). No

81 differences in any physiological or echocardiographic parameters were observed between the

82 *Ncoa4*<sup>−/−</sup> and *Ncoa4*<sup>+/+</sup> mice (Figure 1—figure supplement 2).

83

84 **Attenuation of pressure overload-induced cardiac remodeling in NCOA4-deficient mice**

85 To examine whether NCOA4 is related to cardiac remodeling *in vivo*, *Ncoa4*<sup>+/+</sup> and *Ncoa4*<sup>−/−</sup>

86 mice were subjected to pressure overload employing transverse aortic constriction (TAC) and

87 evaluated four weeks after the operation. Pressure overload increased the left ventricular (LV)

88 chamber size, indicated by the end-diastolic and end-systolic LV internal dimensions, and

89 reduced fractional shortening (an index of contractility) in *Ncoa4*$^{+/+}$ mice compared to sham-

90 operated controls (Figure 1A and B). These pressure overload-induced changes in heart size

91 and function were suppressed in *Ncoa4*$^{-/-}$ mice. The calculated LV mass, LV weight-to-tibia

92 length ratio, and the cross-sectional area of cardiomyocytes, which are parameters for cardiac

93 hypertrophy, were elevated by pressure overload in both *Ncoa4*$^{+/+}$ and *Ncoa4*$^{-/-}$ mice, but those

94 were significantly lower in TAC-operated *Ncoa4*$^{-/-}$ mice than in TAC-operated controls

95 (Figure 1B, C and D). TAC-operated *Ncoa4*$^{+/+}$ mice displayed higher mRNA expression levels

96 of the cardiac remodeling markers, *Nppa*, *Nppb*, and *Myh7* than TAC-operated *Ncoa4*$^{-/-}$ mice

97 (Figure 1—figure supplement 3). Furthermore, the lung weight-to-tibia length ratio, an index

98 of lung congestion, was significantly elevated in TAC-operated *Ncoa4*$^{+/+}$ mice compared to

99 both sham-operated *Ncoa4*$^{+/+}$ and TAC-operated *Ncoa4*$^{-/-}$ mice (Figure 1C). The extent of

100 pressure overload-induced fibrosis in heart sections and the mRNA levels of *Col1a2* and

101 *Col3a1*, markers for fibrosis, in *Ncoa4*$^{-/-}$ mice were lower than in *Ncoa4*$^{+/+}$ mice (Figure 1D

102 and Figure 1—figure supplement 3). There were no differences in echocardiographic

103 parameters between TAC-operated *Ncoa4*$^{+/+}$ and *Ncoa4*$^{-/-}$ mice 4 weeks after TAC (Figure

104 1—figure supplement 4). Thus, the overexpression of Cre recombinase in the heart has no

105 effect on pressure overload-induced cardiac remodeling. Taken together, NCOA4 deficiency

106 attenuated pressure overload-induced cardiac remodeling, including cardiac hypertrophy and

107 dysfunction, chamber dilation, and fibrosis.

108

109 **Attenuation of upregulation of ferritinophagy in pressure-overloaded NCOA4-deficient**

110 **hearts**

111 The level of ferritinophagy in pressure overloaded hearts was then evaluated four weeks after

112 TAC. The protein level of FTH1 was decreased in *Ncoa4*$^{+/+}$ hearts compared to both sham-

113 operated *Ncoa4*$^{+/+}$ and TAC-operated *Ncoa4*$^{-/-}$ hearts (Figure 2A). However, the mRNA level

114  of FTH1 was also decreased in *Ncoa4*^{+/+} hearts (Figure 2B). To clarify the ferritinophagic

115  activity, we evaluated the cardiac phenotypes during an earlier time course after pressure

116  overload when the secondary effect to cardiac remodeling was minimal. Cardiac dysfunction

117  and LV chamber dilation were observed in wild-type *Ncoa4*^{+/+} hearts (Figure 2—figure

118  supplement 1). Both TAC-operated *Ncoa4*^{+/+} and *Ncoa4*^{−/−} mice showed decreased fractional

119  shortening 3 days after surgery compare to the corresponding sham-operated group. However,

120  there was no significant difference in fractional shortening between TAC-operated *Ncoa4*^{+/+}

121  and *Ncoa4*^{−/−} mice, suggesting mild cardiac dysfunction observed in both groups 3 days after

122  TAC was due to acute response to pressure overload. The protein level of FTH1 decreased

123  from postoperative day 5 compared to sham-operated hearts, while the level of *Fth1* mRNA

124  increased 5 and 7 days after TAC and decreased 4 weeks after TAC (Figure 2C and D). NCOA4

125  is responsible for the selective targeting of the ferritin complex to autophagosomes. In the

126  TAC-operated hearts, the number of LC3B (a marker of an autophagosome)- and FTH1-

127  positive dots increased after postoperative day 5 and then declined 4 weeks after TAC (day 7

128  versus 4 weeks, $P < 0.0001$), and that of LAMP2a (a marker of a lysosome)- and FTH1-positive

129  dots increased 7 days after TAC (Figure 2E, F, G and H).

130       The extent of ferritinophagy in *Ncoa4*^{+/+} and *Ncoa4*^{−/−} mice was then evaluated seven days

131  after TAC. The ablation of *Ncoa4* attenuated the downregulation of FTH1 protein and

132  upregulation of *Fth1* mRNA in TAC-operated *Ncoa4*^{+/+} hearts (Figure 3A and B). The number

133  of LC3B- and FTH1-positive dots and the number of LAMP2a- and FTH1-positive dots

134  decreased in TAC-operated *Ncoa4*^{−/−} hearts compared to *Ncoa4*^{+/+} hearts (Figure 3C, D, E and

135  F).

136

137  **Erythropoiesis in NCOA4-deficient mice**

138    To determine whether the failure of cardiomyocyte-specific NCOA4-deficient mice to degrade

139    ferritin in cardiomyocytes affects erythropoiesis, as reported in global NCOA4-deficient mice

140    (Bellelli et al., 2016), we explored the effect of NCOA4 deficiency in the heart on red blood

141    cell parameters (Figure 4—figure supplement 1). There were no significant differences in

142    hematological parameters, serum iron, and transferrin saturation between any groups. Pressure

143    overload reduced serum ferritin compared to the corresponding sham-operated group, but there

144    was no significant difference between TAC-operated $Ncoa4^{+/+}$ and $Ncoa4^{-/-}$ mice. Serum

145    ferritin is both a marker of liver iron stores and acute inflammatory response (Kell et al., 2014).

146    TAC decreased the level of total non-heme iron in both $Ncoa4^{+/+}$ and $Ncoa4^{-/-}$ livers, but there

147    was no significant difference in the level between $Ncoa4^{+/+}$ and $Ncoa4^{-/-}$ mice (Figure 4—

148    figure supplement 2A). TAC increased the serum IL-6 level in both $Ncoa4^{+/+}$ and $Ncoa4^{-/-}$

149    mice, which was higher in $Ncoa4^{+/+}$ than that in $Ncoa4^{-/-}$ (Figure 4—figure supplement 2B). It

150    has been reported that the serum level of IL-6 in the patients with heart failure is related with

151    its severity (Hirota et al., 2004). Thus, the reduced level of serum ferritin level in TAC-operated

152    mice may be due to the reduction in liver iron stores.

153

154    **Iron metabolism in pressure-overloaded NCOA4-deficient hearts**

155    Next, we assessed the effect of pressure overload on iron metabolism in the heart (Figure 4A).

156    Increased free ferrous iron plays a critical role in the Fenton reaction during iron-dependent

157    necrosis. Pressure overload decreased the total non-heme iron content in both $Ncoa4^{+/+}$ and

158    $Ncoa4^{-/-}$ hearts. The level of ferrous iron in $Ncoa4^{+/+}$ hearts was higher than that in $Ncoa4^{-/-}$

159    hearts under pressure overload, whereas the level of ferric iron was lower in $Ncoa4^{+/+}$ hearts

160    than in $Ncoa4^{-/-}$ hearts. The ratio of ferrous iron to FTH1, which represents the non-binding

161    fraction of ferrous iron to FTH1, was higher in TAC-operated $Ncoa4^{+/+}$ hearts than in the sham-

162    operated controls and TAC-operated $Ncoa4^{-/-}$ hearts, suggesting free ferrous iron overload in

163    TAC-operated *Ncoa4*^{+/+} hearts. When iron is limiting iron, regulatory proteins (IRPs) bind to

164    iron regulatory elements (IREs) found in untranslated regions (UTR) of mRNA involved in

165    iron transport and storage (Anderson et al., 2012). IRP binding to IREs found in the 5' UTR of

166    mRNA encoding FTH1, FTL and ferroportin 1 (exports iron out of the cell, also known as

167    solute carrier family 40 member 1; SLC40A1) blocks the initiation of translation. IREs, found

168    in the 3' UTR of transferrin receptor 1 (TFRC; the membrane receptor for iron), divalent metal

169    iron transport (solute carrier family 11 member 2; SLC11A2), cell division cycle 14A

170    (CDC14A), and CDC binding protein kinase alpha (CDC42BPA), bind IRPs to stabilize the

171    mRNA by inhibiting nuclease digestion. The levels of proteins related to intracellular iron

172    metabolism such as IREB2, SLC40A1, and TFRC showed no differences between TAC-

173    operated groups (Figure 4—figure supplement 3A). There were no significant differences in

174    the mRNA levels of *Tfrc*, *Slc11a2*, *Cdc14a*, and *Cdc42bpa* between TAC-operated groups

175    (Figure 4—figure supplement 3B). The binding of IRP with the 5' UTR of *Slc40a1* exhibited

176    no difference between TAC-operated groups (Figure 4—figure supplement 3C). These suggest

177    that IRP system is impaired in TAC-operated *Ncoa4*^{+/+} mice.

178

179    **Lipid oxidation in pressure-overloaded NCOA4-deficient hearts**

180    Lipid peroxidation is a hallmark of iron-dependent necrosis (Dixon et al., 2012). In *Ncoa4*^{+/+}

181    hearts, pressure overload increased the levels of malondialdehyde (MDA) and 4-hydroxy-2-

182    nonenal (4-HNE)-positive area; markers for lipid peroxidation (Ayala et al., 2014) (Figure 4B

183    and Figure 4—figure supplement 4A). In contrast, these markers were attenuated in *Ncoa4*^{−/−}

184    hearts. *Ptgs2* mRNA, a putative marker for ferroptosis (Yang et al., 2014), was increased in

185    TAC-operated *Ncoa4*^{+/+} hearts but not in *Ncoa4*^{−/−} hearts (Figure 4C). There were no significant

186    differences in the antioxidant protein levels of superoxide dismutase 2 and heme oxygenase 1

187    between any groups (Figure 4—figure supplement 4B). The increase in serum troponin T, a

188  marker for necrotic cell death, in TAC-operated *Ncoa4*<sup>+/+</sup> mice was significantly attenuated by

189  *Ncoa4* ablation (Figure 4D). Taken together, these results show that iron-dependent necrosis

190  plays an important role in the development of pressure overload-induced heart failure.

191

192  **Glutathione and glutamine metabolism in pressure-overloaded NCOA4-deficient hearts**

193  The GPX4 protein level was upregulated in TAC-operated $Ncoa4^{+/+}$ hearts compared to the

194  corresponding controls, while ablation of *Ncoa4* suppressed the pressure overload-induced

195  induction of GPX4 (Figure 4E). The levels of total and reduced (GSH) glutathione decreased

196  and oxidized glutathione (GSSG) increased in TAC-operated $Ncoa4^{+/+}$ hearts, resulting in a

197  decreased GSH to GSSG ratio in $Ncoa4^{+/+}$ hearts (Figure 4F). *Ncoa4* ablation normalized the

198  ratio to the sham control level. The cysteine-glutamate antiporter (system $Xc^-$, also known as

199  solute carrier family 7 member 11; SLC7A11) is a key regulator for cystine uptake in cell

200  survival against ferroptosis (Gao et al., 2015). There was no significant difference in the level

201  of *Slc7a11* mRNA or cardiac cystine between TAC-operated $Ncoa4^{+/+}$ and $Ncoa4^{-/-}$ mice

202  (Figure 4—figure supplement 5A and B). The level of glutamate in TAC-operated $Ncoa4^{+/+}$

203  hearts was lower than that in sham-operated $Ncoa4^{+/+}$ or TAC-operated $Ncoa4^{-/-}$ mice (Figure

204  4—figure supplement 5C). L-glutamine uptake is mainly dependent on the receptors

205  SLC38A1, SLC1A5, and SLC7A5 (McGivan et al., 2007), and L-glutamine is converted into

206  glutamate by glutaminase (GLS1 and GLS2). The cardiac glutamine level decreased in TAC-

207  operated $Ncoa4^{+/+}$ hearts compared to the corresponding sham-operated mice and was lower

208  than that in TAC-operated $Ncoa4^{-/-}$ hearts (Figure 4G). There were no significant differences

209  in the mRNA levels of the glutamine transporters or glutaminases between TAC-operated

210  groups (Figure 4—figure supplement 5D). The changes in glutathione metabolism and

211  glutaminolysis in TAC-operated $Ncoa4^{+/+}$ hearts were not as seen in typical ferroptosis.

212

**Isoproterenol-induced cell death in isolated adult cardiomyocytes**

The lipid ROS and labile iron pool during iron-dependent necrosis were further estimated using adult cardiomyocytes isolated from $Ncoa4^{+/+}$ and $Ncoa4^{-/-}$ hearts. The activation of neurohumoral factors such as catecholamine plays an important role in the pathogenesis of heart failure (Shah et al., 2011). The synthetic small-molecule compound erastin inhibits the activity of cysteine–glutamate antiporter, leading to the depletion of GSH (Dixon et al., 2012). High-throughput screening has identified ferrostatin-1 as a potent inhibitor of the accumulation of lipid ROS (Dixon et al., 2012; Friedmann Angeli et al., 2014; Skouta et al., 2014). Erastin or isoproterenol induced cell death in $Ncoa4^{+/+}$ cardiomyocytes, while this occurred to a lesser extent in $Ncoa4^{-/-}$ cardiomyocytes (Figure 5A and Figure 5—figure supplement 1A). Ferrostatin-1 inhibited both erastin- and isoproterenol-induced cardiomyocyte cell death. Treatment of $Ncoa4^{+/+}$ cardiomyocytes with either erastin or isoproterenol resulted in an increase in the cellular and lipid ROS levels, as estimated using the fluorescent probes H2DCFDA and C11-BODIPY, respectively (Dixon et al., 2012) (Figure 5B and C and Figure 5—figure supplement 1B and C). The application of either ferrostatin-1 or $Ncoa4$ ablation prevented the generation of erastin- or isoproterenol-induced cellular and lipid ROS, which is in agreement with a previous report that used HT-1080 cells (Dixon et al., 2012). The labile iron pool level was measured using calcein-acetoxymethyl ester (Yoshida et al., 2019). Erastin and isoproterenol could both increase the level of the labile iron pool in $Ncoa4^{+/+}$ cardiomyocytes, which was attenuated by treatment with ferrostatin-1 (Miotto et al., 2020) (Figure 5D and Figure 5—figure supplement 1D). $Ncoa4$ ablation was effective in reducing the erastin- or isoproterenol-induced upregulation of the labile iron pool. Isoproterenol decreased the protein level of FTH1 in an NCOA4-dependent manner (Figure 5E). A small molecule, RSL3, is another ferroptosis inducer, which binds and inhibits GPX4 (Yang et al.,

237 2015). RSL3 induced cardiomyocyte death, which was attenuated by *Ncoa4* ablation or

238 ferrostatin-1 treatment (Figure 5—figure supplement 2).

239

**Attenuation of the development of cardiac remodeling by ferrostatin-1**

241 To examine the involvement of iron-dependent necrosis in the pathogenesis of heart failure and

242 whether iron-dependent necrosis is a therapeutic target for the disease, wild-type C57BL/6J

243 mice received an intraperitoneal daily injection of ferrostatin-1. Four weeks after TAC, saline-

244 administered mice exhibited LV chamber dilation and cardiac dysfunction (Figure 6A and B).

245 Ferrostatin-1 administration significantly reduced the LV chamber size and improved cardiac

246 function in TAC-operated mice. Pressure overload-induced increases in LV mass and weight,

247 the cross-sectional area of cardiomyocytes, and remodeling markers such as *Nppa*, *Nppb* and

248 *Myh7* mRNAs were significantly attenuated in ferrostatin-1-treated hearts (Figure 6C and D

249 and Figure 6—figure supplement 1A). TAC-operated saline-treated mice exhibited cardiac

250 fibrosis, which was diminished by ferrostatin-1 (Figure 6D and Figure 6—figure supplement

251 1A). Thus, ferrostatin-1 prevented the development of pressure overload-induced

252 cardiomyopathy. TAC-operated control mice showed increased lipid ROS and *Ptgs2* mRNA,

253 which was inhibited by the administration of ferrostatin-1 (Figure 6E and F and Figure 6—

254 figure supplement 1B). Taken together, these findings indicate that iron-dependent necrosis

255 was involved in the pathogenesis of pressure overload-induced heart failure in the wild-type

256 mice.

257 To examine whether iron-dependent cell death is downstream of NCOA4, $Ncoa4^{-/-}$ mice

258 received an intraperitoneal daily injection of ferrostatin-1. Four weeks after TAC, there was no

259 significant difference in the extent of cardiac remodeling between saline- and ferrostatin-1-

260 treated mice (Figure 6—figure supplement 2).

**Discussion**

Our data indicate that there is no cardiomyocyte-autonomous requirement for NCOA4 during normal embryonic development. Furthermore, the NCOA4-mediated pathway does not appear to be required for normal heart growth in the postnatal period. We found that NCOA4-dependent ferritinophagy is activated for degradation of ferritin in the heart in response to pressure overload and is detrimental in the stressed heart. The release of ferrous iron from ferritin leads to the increase in lipid ROS, cardiac necrosis, and heart failure.

We observed the reduction of FTH1 protein level in $Ncoa4^{+/+}$ hearts four weeks after TAC as we previously reported (Omiya et al., 2009). Because the mRNA level of FTH1 was also decreased, it was not conclusive that the decrease in FTH1 was due to increased ferritinophagy. Our study analyzing the heart during an earlier time course after pressure overload showed that the protein level of FTH1 decreased along with an increase in the level of $Fth1$ mRNA, suggesting that the downregulation of FTH1 is due to its degradation. In the TAC-operated hearts, FTH1 was recruited in autophagosomes or autolysosomes and this recruitment was NCOA4-dependent. These findings confirmed that pressure overload induces the activation of NCOA4-mediated ferritinophagy, which is detrimental to the heart. The labile iron pool and oxidative stress are known to increase $Fth1$ mRNA (Arosio et al., 2009), that may explain the increased level of $Fth1$ mRNA at the early time points after pressure overload. The detrimental effect of FTH1 downregulation on cardiac function is supported by a recent report showing that mice lacking FTH1 in cardiomyocytes increased oxidative stress, resulting in mild cardiac dysfunction upon aging (Fang et al., 2020).

Iron is essential for the survival of the cells, as it serves as a cofactor in the biochemical processes such as oxygen storage, oxidative phosphorylation, and enzymatic reaction (Andrews et al., 2007). Intracellular iron levels are maintained by NCOA4-dependent ferritin degradation (Mancias et al., 2014). While ferritin supplies iron for mitochondrial function

286 (Fujimaki et al., 2019), it protects the cell against free radical generation via the Fenton reaction

287 (Papanikolaou et al., 2005). These suggest the importance of NCOA4 in intracellular iron

288 homeostasis and a double-edged sword role of ferritinophagy. Our study presented here

289 indicate that NCOA4-mediated ferritinophagy is pathologic for the heart in response to

290 pressure overload by activating iron-dependent cell death. In addition, $Ncoa4^{-/-}$ mice showed

291 normal cardiac function at baseline as well as under hemodynamic stress, suggesting that iron

292 derived from ferritin degradation is not necessary for cardiac homeostasis or some other transit

293 pools of iron such as low-molecular-weight chelates including citrate, ATP, AMP or

294 pyrophosphate, may compensate the loss of NCOA4 in the heart (Papanikolaou et al., 2005).

295 Why does the maladaptive hyperactivation of ferritinophagy occur in pressure overloaded

296 hearts? NCOA4-dependent ferritinophagy is regulated by intracellular iron (Dowdle et al.,

297 2014; Mancias et al., 2014). However, the precise activation mechanism of ferritinophagy–cell

298 death pathway in response to hemodynamic stress remains to be elucidated. We found that $\beta_1$-

299 adrenergic agonist, isoproterenol, induced cardiomyocyte death in which the NCOA4-

300 dependent pathway, the generation of lipid ROS and increased labile iron pool are involved. In

301 addition, we showed that isoproterenol induces ferritinophagy. Thus, the downstream signaling

302 pathways of $\beta_1$-adrenergic receptors activates ferritinophagy and resultant cell death. Another

303 possibility is that isoproterenol induces intracellular iron deficiency in cardiomyocytes to lead

304 to ferritinophagy. However, the expression level of FTH1 was maintained in cardiomyocyte-

305 specific IREB1/2-deficient hearts with iron deficiency (Haddad et al., 2016), suggesting that

306 iron deficiency may not directly induce FTH1 degradation in cardiomyocytes. It is also possible

307 that NCOA4 may associate with NRF2/HO-1 and VDACs-induced mitochondrial dysfunction

308 pathways in ferroptosis-induced cardiomyocytes death and heart failure (Li et al., 2020). It has

309 been reported that NCOA4 has association with mitochondria iron-overload in cardiomyocyte

310 hypertrophy pathophysiology (Tang et al. 2019). Although NCOA4-mediated ferritin

14

311  degradation contributes to maintain mitochondrial function through iron supply (Fujimaki et

312  al., 2019), excessive ferritinophagy may induce cardiomyocyte hypertrophy and cell death.

313  Further studies are necessary to elucidate molecular mechanism underlying NCOA4-mediated

314  cardiomyocyte death and heart failure.

315  Although pressure overload decreased the level of ferrous iron in the heart, the level of

316  ferrous iron in $Ncoa4^{+/+}$ hearts was higher than that in $Ncoa4^{-/-}$ hearts. The calculated non-

317  binding fraction of ferrous iron to FTH1 was higher in TAC-operated $Ncoa4^{+/+}$ hearts. To

318  confirm the increased level of ferrous iron in pressure overloaded $Ncoa4^{+/+}$ hearts, we measured

319  the labile iron pool in isolated cardiomyocytes. Erastin and isoproterenol could both increase

320  the level of the labile iron pool in $Ncoa4^{+/+}$ cardiomyocytes, which was attenuated by $Ncoa4$

321  ablation. These suggest labile iron overload induced by activation of ferritinophagy in stressed

322  cardiomyocytes, even though the pressure-overloaded $Ncoa4^{+/+}$ mice exhibited decreased total

323  cardiac iron.

324  Deregulation of programmed cardiomyocyte death has been reported to play an important

325  role in the pathogenesis of heart failure (Whelan et al., 2010). While apoptosis is the best-

326  studied form of programmed cell death, there are also non-apoptotic programmed cell death.

327  Necroptosis and iron-dependent necrosis are two distinct regulated necrotic cell death. We

328  observed increases in lipid peroxidation in TAC-operated $Ncoa4^{+/+}$ hearts but not in $Ncoa4^{-/-}$

329  hearts. In addition, ferrostatin-1 attenuated the development of pressure overload-induced

330  cardiac remodeling. Taken together, these results show that iron-dependent necrosis plays an

331  important role in the development of pressure overload-induced heart failure. Ferrostatin-1 did

332  not provide additional protection from pressure overload-induced cardiac remodeling in

333  $Ncoa4^{-/-}$ mice, suggesting that iron-dependent cardiomyocyte death is downstream of NCOA4-

334  mediated ferritinophagy. GPX4 inhibits the formation of lipid peroxidation and ferroptosis

335  (Yang et al., 2014), while glutaminolyis is required for the execution of ferroptosis. We found

that *Ptgs2* mRNA, a putative marker for ferroptosis was upregulated TAC-operated *Ncoa4*<sup>+/+</sup> hearts, however, the GPX4 protein level was upregulated, while glutamate and glutamine were downregulated in TAC-operated *Ncoa4*<sup>+/+</sup> hearts. The mRNA of *Slc7a11* in system Xc$^-$ and cystine showed no difference between TAC-operated *Ncoa4*<sup>+/+</sup> and *Ncoa4*<sup>-/-</sup> hearts. These results suggest that the pressure overload-induced increase in GPX4 was compensatory to prevent iron-dependent necrosis, and insufficient induction of GPX4 may lead to the increase in lipid ROS and the downregulation of glutamine or glutamate was also a compensatory mechanism to inhibit iron-dependent necrosis. ROS have a variety of physiological and pathological functions depending on their source, species and local concentration, local antioxidant environment, and possibly the disease stage (Papaharalambus et al., 2007). Intensive studies have implicated ROS in the development of cardiovascular pathology including cardiac remodeling (Ponikowski et al., 2016). However, the failure of clinical trials using antioxidants requests more precise understanding of the sources and contribution of ROS in heart failure. Our study indicates that lipid ROS derived from ferritinophagy and the Fenton reaction plays an important role in the pathogenesis of heart failure. Thus, our study supports the notion that inhibiting lipid peroxidation is cardioprotective during pressure overload.

Iron deficiency is a common condition affecting approximately 50% of patients with heart failure (Lavoie, 2020). Clinical trials have demonstrated the symptomatic benefit of treating iron-deficient heart failure patients with intravenous iron supplementation (Anker et al., 2009; Ghafourian et al., 2020). However, heart failure patients may have underlying myocardial iron overload (Ghafourian et al., 2020; Sawicki et al., 2015). In addition, a high-iron diet caused severe cardiac dysfunction in cardiomyocyte-specific FTH1-deficient mice (Fang et al., 2020). These raises concerns about the safety of the prolonged use of iron supplementation in heart failure patients. The long-term safety of iron supplementation in heart failure patients must be

360     determined. Our results do not contradict the clinical trials but rather imply a potential role for

361     reducing iron-dependent cell death in patients with heart failure.

362         In summary, the data presented here reveal a novel mechanism underlying the pathogenesis

363     of heart failure. Iron-dependent cardiomyocyte death plays an important role in the

364     development of pressure overload-induced heart failure. The inhibition of iron-dependent

365     cardiomyocyte death can be a novel therapeutic mechanism for patients with heart failure.

**Methods**

**Animal studies**

All procedures were carried out in accordance with the King's College London Ethical Review Process Committee and the UK Home Office (Project License No. PPL70/8889) and were performed in accordance with the Guidance on the Operation of the Animals (Scientific Procedures) Act, 1986 (UK Home Office).

**Antibodies**

The following antibodies were used in this study: monoclonal mouse antibody to NCOA4 (Sigma-Aldrich, SAB1404569, Lot: HC071-1F11, 1/1,000), polyclonal rabbit antibody to FTH1 (Cell Signaling Technology, 3998, Lot: 2, for western blots, 1/1,000; for immunofluorescence, 1/100), monoclonal mouse antibody to LC3B (Cell Signaling Technology: 83506, Lot: 1, 1/100), monoclonal rat antibody to LAMP2a (Abcam: ab13524, Lot: GR3317907-1, 1/100), monoclonal rat antibody to GPX4 (Millipore: MABS1274, Lot: Q2633070, 1/1,000), polyclonal rabbit antibody to 4-HNE (Millipore: 393207, Lot: 3167038, 1/500), polyclonal rabbit antibody to IREB2 (Thermo Fisher Scientific: PA1-16543, Lot: TK2666362A, 1/250), polyclonal rabbit antibody to SLC40A1 (Alpha Diagnostic International: MTP11-A, Lot: 1169899A3-L, 1/1,000), monoclonal mouse antibody to TFRC (Thermo Fisher Scientific: 13-6800, Lot: TI275369, 1/1,000), polyclonal rabbit antibody to SOD2 (Abcam: ab13534, Lot: GR33618-66, 1/1,000), polyclonal rabbit antibody to HO-1 (Enzo Life Sciences: ADI-SPA-895, Lot: 03301708, 1/1,000), monoclonal mouse antibody to GAPDH (Sigma-Aldrich: G8795, Lot: 056M4856V, 1/10,000).

**Generation of cardiomyocyte-specific NCOA4-deficient mice**

390    The *Ncoa4* gene-targeting vector was constructed using mouse C57BL/6J genomic DNA

391    (Misaka et al., 2018). The targeting vector was electroporated into ES cells (F1; SVJ129 and

392    C57BL/6J), and the transfected ES clones were selected for neomycin resistance according to

393    standard protocols. The neomycin-resistant ES clones with targeted homologous

394    recombination were screened by PCR and further confirmed by Southern blotting. Circular

395    pCAG-Flpe plasmid and pPGK-Puro plasmid were electroporated into the selected ES clones,

396    and the transfected ES clones were selected for puromycin resistance according to standard

397    protocols. The neomycin cassette-excised ES clones were screened by PCR. Southern blotting

398    and karyotyping analyses were performed to obtain ES clones exhibiting the desired

399    homologous recombination and normal karyotype. These targeted ES clones were injected into

400    blastocyst C57BL/6J mouse embryos to generate chimeric mice. The chimeric mice were

401    crossed with C57BL/6J mice to validate germ line transmission. We generated mice with the

402    floxed *Ncoa4* allele and crossed them with transgenic mice expressing α-myosin heavy chain

403    promoter-driven Cre recombinase (Myh6-Cre) to obtain cardiomyocyte-specific NCOA4-

404    deficient mice (*Ncoa4*$^{\text{flox/flox}}$;Myh6-Cre$^{+}$) (Nishida et al., 2004). *Ncoa4*$^{\text{flox/flox}}$;Myh6-Cre$^{-}$

405    littermates were used as controls. The mice had access to food and water *ad libitum*.

406

**Immunoprecipitation and western blot analysis**

408    To evaluate NCOA4 protein expression level in hearts, the protein was immunoprecipitated

409    with an anti-NCOA4 antibody, followed by immunoblot with the antibody. One hundred μg

410    protein homogenates with lysis buffer (50 mmol/L Tris-HCl, 50 mmol/L NaCl, 1 mmol/L

411    EDTA, 1% NP-40, a protease inhibitor cocktail, pH 7.4) were precleared with 20 μL of

412    magnetic beads-coupled protein G (Thermo Fisher Scientific, 1004D). Precleared homogenates

413    were subjected to immunoprecipitation using one μg of the anti-NCOA4 antibody (Sigma-

414    Aldrich, SAB1404569) or mouse immunoglobulin G (IgG; Santa Cruz biochemistry, sc-2025)

415 and 40 μL of magnetic beads-coupled protein G at four °C for two hours. The precipitated

416 complexes were washed three times with lysis buffer. Protein homogenates with lysis buffer

417 were extracted from the left ventricles. The precipitated complexes or 5–15 μg of total protein

418 homogenates were subjected to Western blot analysis. After incubation with secondary

419 antibody, the blot was developed with an infrared imaging system (ODYSSEY CLx; LI-COR

420 Biosciences). Image Studio software (LI-COR Biosciences) was used for quantitative analysis

421 to evaluate protein expression levels.

422

423 **Real-time quantitative reverse transcription PCR**

424 Total RNA was isolated from the left ventricles using RNeasy Fibrous Tissue Mini Kit

425 (QIAGEN). The mRNA expression levels were determined by quantitative reverse

426 transcription polymerase chain reaction (PCR) using SuperScript IV reverse transcriptase

427 (Thermo Fisher Scientific Inc) for reverse transcription and a PowerUp SYBR Green PCR

428 Master Mix (Thermo Fisher Scientific) for the quantitative PCR reaction with the following

429 PCR primers: forward 5'–CTATATCCAGGTGCCAGAGCAG–3' and reverse 5'–

430 TTGCTTACAAGAAGCCACTCAC–3' for *Ncoa4*, forward 5'–

431 TGGAGTTGTATGCCTCCTACG–3' and reverse 5'–

432 TGGAGAAAGTATTTGGCAAAGTT–3' for *Fth1*, forward 5'–

433 CAGACAACATAAACTGCGCCTT–3' and reverse 5'–

434 GATACACCTCTCCACCAATGACC–3' for *Ptgs2*, forward 5'-

435 TGGCCAGCAAGATTGTGGAGAT-3' and reverse 5'–TTTGCGGGTGAAGAGGAAGT–

436 3' for *Slc1a5*, forward 5'–ATGGAGTGTGGCATTGGCTT–3' and reverse 5'–

437 TGCATCAGCTTCTGGCAGAGCA–3' for *Slc7a5*, forward 5'–

438 TCTACAGGATTGCGAACATCT–3' and reverse 5'–

439 CTTTGTCTAGCATGACACCATCT–3' for *Gls1*, forward 5'–

440 AGCGTATCCCTATCCACAAGTTCA–3' and reverse 5'–

441 GCAGTCCAGTGGCCTTCAGAG–3' for *Gls2*, forward 5'–TCGTCTTGGCCTTTTGGCT–

442 3' and reverse 5'–TCCAGGTGGTCTAGCAGGTTCT–3' for *Nppa*, forward 5'–

443 AAGTCCTAGCCAGTCTCCAGA–3' and reverse 5'–GAGCTGTCTCTGGGCCATTTC–3'

444 for *Nppb*, forward 5'–ATGTGCCGGACCTTGGAAG–3' and reverse 5'–

445 CCTCGGGTTAGCTGAGAGATCA–3' for *Myh7*, forward 5'–

446 ACGCGGACTCTGTTGCTGCT–3' and reverse 5'–GCGGGACCCCTTTGTCCACG–3' for

447 *Col1a2*, forward 5'–CCCGGGTGCTCCTGGACAGA–3' and reverse 5'–

448 CACCCTGAGGACCAGGCGGA–3' for *Col3a1*, forward 5'–

449 TGCAATCTGCATCTCCATGGCT–3' and reverse 5'–AAGCAGGAGAGGGCAACAAA–

450 3' for *Slc7a11*, forward 5'–TGGAATCCCAGCAGTTTCTT–3' and reverse 5'–

451 GCTGCTGTACGAACCATTTG–3' for *Tfrc*, forward 5'–

452 GGCTTTCTTATGAGCATTGCCTA–3' and reverse 5'–GGAGCACCCAGAGCAGCTTA–

453 3' for Slc11a2, forward 5'–TGGACCTCTGAACTTGGCAAT–3' and reverse 5'–

454 AGATGACGGCATAAGCACCTAT–3' for *Cdc14a*, forward 5'–

455 TTTCCACCTAAGCGCAAGACT–3' and reverse 5'–ATGACATGAGAACCCACAGA–3'

456 for *Cdc42bpa*, and forward 5'–ATGACAACTTTGTCAAGCTCATTT–3' and reverse 5'–

457 GGTCCACCACCCTGTTGCT–3' for *Gapdh*. PCR standard curves were constructed using

458 the corresponding cDNA and all data were normalized to the *Gapdh* mRNA content and are

459 expressed as the fold increase over the control group.

460

461 **Transverse aortic constriction (TAC) and echocardiography**

462 The 8–12-week-old male mice were subjected to TAC using a 26-gauge needle or to a sham

463 surgery, as previously reported (Omiya et al., 2020). In TAC, a small piece of 6-0 silk suture

464 was placed between the innominate and left carotid arteries. Three loose knots were tied around

the transverse aorta, and a 26-gauge needle was placed parallel to the transverse aorta. The

knots were tied quickly against the needle and the needle was removed promptly to yield a 26-

gauge stenosis. Sham surgeries were identical except for the aortic constriction.

Echocardiography was conducted with a Vevo 2100 system (Visual Sonics) on conscious mice

(Omiya et al., 2020). Non-invasive measurement of the tail blood pressure was also performed

on conscious mice using a NP-NIBP Monitor for mice and rats (Muromachi Kikai), as

previously described (Omiya et al., 2020).

**Histological analysis**

Left ventricle samples were embedded in OCT compound (Thermo Fisher Scientific Inc) and

then immediately frozen in liquid nitrogen. The samples were sectioned into 5-μm thick

sections. The sections were fixed with acetone for Hematoxylin–eosin staining and Masson's

trichrome staining, with 4% paraformaldehyde for wheat germ agglutinin staining and with

Bouin's solution for 4-HNE staining. Hematoxylin–eosin staining and Masson's trichrome

staining (Masson's Trichrome Stain Kit, Polysciences Inc) were performed on serial sections.

For wheat germ agglutinin staining, heart samples were stained with fluorescein

isothiocyanate-conjugated lectin (Sigma, L4895) to measure the cross-sectional area of

cardiomyocytes. For 4-HNE staining, rabbit anti-4-HNE antibody or control rabbit IgG

(Abcam, ab37415) were used as primary antibody, and avidin-peroxidase (Vectastain Elite

ABC Kit; Vector Laboratories Inc) and the DAB Peroxidase Substrate Kit (Vector Laboratories

Inc) were applied, followed by counterstaining with hematoxylin as described previously

(Shigemiki Omiya et al., 2020). Images were captured by an All-in-one fluorescence

microscope (BZ-X700, Keyence). Quantitative analyses of the fibrosis fraction and 4-HNE

positive area were examined in whole left ventricles and cardiomyocyte cross-sectional areas

489 was examined in five different areas per section and measured using ImageJ (National Institutes

490 of Health; Version 1.51r).

491

492 **Immunofluorescence microscopy**

493 The OCT-compound embedded frozen left ventricle samples were used to detect LC3B-FTH1

494 and LAMP2a-FTH1 co-localization dots. The samples were sectioned into 5-μm thick sections

495 and fixed with 4% paraformaldehyde for immunohistochemical fluorescence staining. The

496 samples were blocked with 10% normal donkey serum (Abcam, ab7475) to detect LC3B-FTH1

497 co-localization and with 10% normal donkey serum and 10% normal goat serum (Abcam,

498 ab7481) to detect LAMP2a-FTH1 co-localization. The primary antibodies were rabbit anti-

499 FTH1, mouse anti-LC3B, and rat anti-LAMP2a. The secondary antibodies were Alexa Fluor

500 488 donkey-anti-mouse (Thermo Fisher Scientific: A21202, 1/500), Alexa Fluor 568 donkey-

501 anti-rabbit (Thermo Fisher Scientific: A10042, 1/500), and Alexa Fluor 488 goat-anti-rat

502 (Thermo Fisher Scientific: A11006, 1/500). DAPI (ProLong Gold Antifade Reagent with

503 DAPI; Life Technologies: P36935) was used to detect nuclei. Micrographs were acquired using

504 a Nikon Eclipse Ti inverted microscope (Nikon) equipped with a Yokogawa CSU-X1 spinning

505 disk unit (Yokagawa) and an Andor EMMCD camera (Andor Technology) using a 100x oil

506 immersion objective lens. The co-localization dots were quantified by counting the number of

507 LC3B-FTH1- or LAMP2a-FTH1-positive dots in 10 different areas (magnification 1,000x) per

508 section.

509

510 **Measurement of hematological parameters, serum ferritin, serum iron, transferrin**

511 **saturation, serum troponin T, and serum IL-6**

512 Blood samples were obtained from the inferior vena cava in anesthetized mice. Full blood count

513 and reticulocyte count were measured at Pinmoore Animal Laboratory Services Limited. Blood

samples were centrifuged for 30 minutes at 850 x g to isolate serum fraction. Serum ferritin levels were measured using a Mouse Ferritin ELISA Kit (FTL) (Abcam, ab157713) according to the manufacturer's protocols. Serum iron levels and transferrin saturation were measured using Pointe Scientific Iron/TIBC Reagents (Pointe Scientific, 23-666-320) according to the manufacturer's protocols. Serum troponin T levels were measured using the ELISA Kit for Troponin T Type 2, Cardiac (TNNT2) (Cloud-Clone, SED232Mu) according to the manufacturer's protocols. Serum IL-6 levels were measured using the ELISA Kit for Mouse IL-6 (R&D Systems, M6000B) according to the manufacturer's protocols.

**Measurement of total non-heme, ferrous, and ferric iron levels in hearts**

Total non-heme, ferrous, and ferric iron in hearts or liver were analyzed using an Iron Assay Kit (Abcam, ab83366) according to the manufacturer's protocols. Briefly, the whole heart was perfused with saline and 10–20 mg of left ventricle tissue was homogenized in Iron Assay Buffer. The supernatant without the insoluble fraction was separated by centrifugation and used for analysis. A microplate reader was used to measure the absorbance at OD 593 nm. The level of ferric iron was calculated by subtracting ferrous iron from total non-heme iron. The ratio of the ferrous iron level to the FTH1 protein level was calculated to estimate non-binding fraction of ferrous iron to FTH1. The FTH1 protein level for sham-operated $Ncoa4^{+/+}$ estimated as Western blot analysis in hearts was set to 1.

**Measurement of malondialdehyde (MDA) in hearts**

The amount of MDA in the hearts was measured using a Lipid Peroxidation (MDA) Assay Kit (Abcam, ab118970) according to the manufacturer's protocols. Briefly, 10–20 mg of fresh left ventricle tissue was homogenized in Lysis Solution containing butylated hydroxytoluene. The insoluble fraction was removed by centrifugation, and the supernatant was used for analysis.

539  The supernatants were mixed with thiobarbituric acid (TBA) solution reconstituted in glacial

540  acetic acid and then incubated at 95°C for 60 minutes. The supernatants containing MDA-TBA

541  adduct were added into a 96-well microplate for analysis. A microplate reader was used to

542  measure the absorbance at OD 532 nm.

543

544  **Glutathione quantification**

545  Oxidized glutathione (GSSG) and total glutathione in hearts were analyzed using a GSSG/GSH

546  Quantification Kit (Dojindo, G257) according to the manufacturer's protocols. Briefly, 20–30

547  mg of fresh left ventricle tissue was homogenized in 5% 5-sulfosalicylic acid (SSA), and the

548  insoluble fraction was removed by centrifugation. The resultant supernatant was added to

549  double-deionized $H_2O$ (dd$H_2O$) to reduce the SSA concentration to 0.5% for the assay. A

550  microplate reader was used to measure absorbance at OD 415 nm. The concentration of reduced

551  glutathione (GSH) was calculated by subtracting 2x GSSG from the total glutathione

552  concentration.

553

554  **Measurement of glutamine and glutamate concentration in hearts**

555  The glutamine concentration in hearts was analyzed using a Glutamine Assay Kit (Abcam,

556  ab197011) according to the manufacturer's protocols. Briefly, 10–20 mg of fresh left ventricle

557  tissue was homogenized in ice-cold Hydrolysis Buffer, and the insoluble fraction was removed

558  by centrifugation. The supernatant was added to perchloric acid (PCA). After five minutes

559  incubation on ice, the samples were centrifuged and the supernatants were transferred into new

560  tubes. To remove excess PCA, potassium hydroxide was added to the supernatant and the

561  precipitated PCA was removed by centrifugation. A microplate reader was used to measure the

562  absorbance at OD 450 nm. The glutamate concentration in hearts was analyzed using a

563  Glutamate Assay Kit (Abcam, ab83389) according to the manufacturer's protocols. Briefly,

564    10–20 mg of fresh left ventricle tissue was homogenized in ice-cold Assay Buffer, and the

565    insoluble fraction was removed by centrifugation. The supernatants were added into a 96-well

566    microplate for analysis. A microplate reader was used to measure the absorbance at OD 450

567    nm.

568

**Free amino acid analysis by high–performance liquid chromatography (HPLC)**

570    The mouse hearts were grinded with liquid nitrogen. Proteins were precipitated out from the

571    mouse hearts using a 5% SSA solution, filtered and then measured by ion exchange

572    chromatography with post column ninhydrin derivatization using a Biochrom 30+ amino acid

573    analyzer with a lithium buffer system (Biochrom). EZChrom Elite software (Version 3.3.2.)

574    was used for analysis.

575

**Electrophoretic mobility–shift assay (EMSA)**

577    Electrophoretic mobility–shift assay (EMSA) was performed using Electrophoretic Mobility-

578    Shift Assay kit (Invitrogen: E33075), according to the manufacturer's instructions. The

579    following IRE containing mouse *Slc40a1* 5' UTR with T7 promoter was synthesized by

580    Integrated DNA Technologies (gBlocks Gene Fragments): 5'–

581    TAATACGACTCACTATAGGGGAGAGCAGGCTCGGGGTCTCCTGCGGCCGGTGGA

582    TCCTCCAACCCGCTCCCATAAGGCTTTGGCTTTCCAACTTCAGCTACAGTGTTAGC

583    TAAGTTTGGAAAGAAGACAAAAGAAGACCCCGTGACAGCTTTGCTGTTGTTGTT

584    TGCCTTAGTTGTCCTTTGGGGTCTTTCGGCATAAGGCTGTTGTGCTTATACTGGTG

585    CTATCTTCGGTTCCTCTCACTCCTGTGAACAAGCTCCCGGGCAAGAGCAGCTAAA

586    GCTACCAGCAT–3'. The 287 bp fragment was cloned into pCR-Blunt II-TOPO (Invitrogen:

587    451245). This plasmid DNA containing the mouse *Slc40a1* 5' UTR was linearized by EcoRI

588    and transcribed using HiScrib T7 Quick High Yield RNA Synthesis Kit (New England Biolabs:

589    E2050S). Twenty μg of total protein homogenates from mouse heart were incubated with 50

590    ng of RNA oligonucleotides and subjected to electrophoresis on 6% nondenaturing

591    polyacrylamide gels. The gels were stained using SYBR Green EMSA stain and captured using

592    ChemiDoc-It Imaging Systems with Transilluminator (UVP).

593

594    **Isolation of mouse adult cardiomyocytes**

595    Adult cardiomyocytes were isolated from 8–12-week-old male mice using a Langendorff

596    system and cultured (Oka et al., 2012). Briefly, after *Ncoa4$^{+/+}$* or *Ncoa4$^{-/-}$* male mice had been

597    deeply anesthetized, the heart was quickly excised, cannulated via the aorta, and perfused at

598    constant flow. Hearts were first perfused for one minute at 37°C with a perfusion buffer

599    containing 120 mM NaCl, 5.4 mM KCl, 1.6 mM MgCl2, 1.2 mM NaH$_2$PO$_4$, 5.6 mM glucose,

600    20 mM NaHCO3 and 5 mM taurine (Sigma-Aldrich), followed by collagenase buffer

601    containing 1.2 mg/ml collagenase type 2 (Worthington Biochemical Corporation), and 0.016

602    mg/ml protease type XIV (Sigma-Aldrich: P-5147). After collagenase and protease digestion,

603    the supernatant containing the dispersed myocytes was filtered into a sterilized tube and gently

604    centrifuged at 20 x g for three minutes. The cell pellet was then promptly resuspended in

605    perfusion buffer containing 200 μM Ca$^{2+}$. The cardiomyocytes were pelleted by gravity for 10

606    minutes, the supernatant was aspirated, and the cardiomyocytes were resuspended in perfusion

607    buffer containing 500 μM Ca$^{2+}$. The final cell pellet was suspended in perfusion buffer

608    containing 1 mM Ca$^{2+}$, and an appropriate amount of rod-shaped cardiomyocytes was then

609    suspended in Minimum Essential Medium Eagle (MEM) (Sigma-Aldrich: M5650)

610    supplemented with 2.5% fetal bovine serum, 2 mM L-glutamine, 100 U/ml penicillin, and 100

611    g/ml streptomycin (Sigma-Aldrich: G6784) and plated onto laminin (Invitrogen: 23017-015)-

612    coated plates. After one hour of incubation in the culture medium, the cardiomyocytes were

613    cultured in MEM (glutamine- and phenol red-free, Gibco: 51200038) supplemented with 1x

614    MEM non-essential amino acids solution (Gibco: 11140035), 100 μg/ml bovine serum

615    albumin, insulin (10 mg/l)-transferrin (5.5 mg/l)-sodium selenite (6.7 μg/l) media supplement

616    (ITS; Gibco: 41400045), 2 mM L-glutamine, 100 U/ml penicillin, and 100 g/ml streptomycin

617    (Sigma-Aldrich: G6784).

618

619    **Cell death and ROS production**

620    Cardiomyocyte death was estimated using a Live/Dead Viability/Cytotoxicity Assay Kit

621    (Invitrogen). Isolated adult cardiomyocytes were pre-treated with or without 10 μM ferrostatin-

622    1 (Sigma Aldrich: SML0583) for 30 minutes before treatment with 10 or 20 μM erastin (Sigma

623    Aldrich: E7781), 10 or 100 μM isoproterenol (Sigma Aldrich: I5627), or 2 or 5 μM RSL3

624    (Sigma Aldrich: SML2234). The cells were then stimulated with or without ferrostatin-1 in the

625    medium for four hours. After stimulation, the cells were stained with 1 mM calcein-AM

626    (Invitrogen: C1430) and 2 μM ethidium homodimer-1 (Invitrogen: E1169) in the medium at

627    37°C for 10 minutes. The cells were washed three times using the medium and observed under

628    a microscope (BZ-X700, Keyence). ROS production was measured by applying several

629    indicators. After treatment with erastin or isoproterenol with or without ferrostatin-1, cells were

630    stained with 25 μM 2', 7'-dichlorodihydrofluorescein diacetate (H2DCFDA; Invitrogen:

631    D399) or C11-BODIPY (Invitrogen: D3861) in medium at 37°C for 10 minutes. The cells were

632    then washed with the medium. ROS production was quantified using a fluorescence microplate

633    reader.

634

635    **Measurement of the labile iron pool**

636    The labile iron pool in the isolated adult cardiomyocytes was measured by the calcein-AM

637    method (Yoshida et al., 2019). After treatment with indicated concentration of erastin or

638    isoproterenol with or without 30 minutes treatment of 10 μM ferrostatin-1, cells were incubated

639 with 1 μM calcein-AM at 37°C for 10 minutes and then washed three times with the medium.

640 The fluorescence was measured using a fluorescence microplate reader. Then, the cells were

641 treated with 10 μM pyridoxal isonicotinoyl hydrazine (PIH; Abcam: ab145871) at 37°C for 10

642 minutes, and washed three times with the medium. The fluorescence was measured again in a

643 fluorescence microplate reader. The changes in fluorescence (ΔF) upon PIH treatment was

644 calculated for each sample.

645

**Administration of ferrostatin-1**

647 Twenty-five mg of ferrostatin-1 was dissolved in 2.5 mL of DMSO, and then diluted with

648 saline to the intended concentration. The final DMSO concentration was 5%. One day before

649 and after TAC operation, the C57BL/6J mice or $Ncoa4^{flox/flox}$;Myh6-Cre$^+$ mice received an

650 intraperitoneal injection of one mg/kg body weight ferrostatin-1 or saline containing 5%

651 DMSO and every day thereafter. Following saline or ferrostain-1 injection, the mice were

652 randomly assigned into sham and TAC groups.

653

**Statistics**

655 The results are shown as the mean ± SEM. Statistical analyses were performed using GraphPad

656 Prism 8 (GraphPad Software). Paired data were evaluated by unpaired, two-tailed Student's *t*-

657 test. A one-way analysis of variance (ANOVA) followed by Tukey–Kramer's post hoc test was

658 used for multiple comparisons. A two-way ANOVA followed by Tukey's multiple comparisons

659 test was used for the *in vitro* experiments. $P < 0.05$ was considered to be statistically significant.

660

673     **Disclosures**

674     The authors declare no conflict of interests.

675

676     **<u>Figure Supplements</u>**

677     Figure 1—figure supplement 1

678     Figure 1—figure supplement 2

679     Figure 1—figure supplement 3

680     Figure 1—figure supplement 4

681     Figure 2—figure supplement 1

682     Figure 4—figure supplement 1

683     Figure 4—figure supplement 2

684     Figure 4—figure supplement 3

685     Figure 4—figure supplement 4

686    Figure 4—figure supplement 5

687    Figure 5—figure supplement 1

688    Figure 5—figure supplement 2

689    Figure 6—figure supplement 1

690    Figure 6—figure supplement 2

691

692    **<u>Source Data Files</u>**

693    Figure 1—Source Data 1

694    Figure 2—Source Data 1

695    Figure 3—Source Data 1

696    Figure 4—Source Data 1

697    Figure 5—Source Data 1

698    Figure 6—Source Data 1

699    Figure 1—figure supplement 1—Source Data 1

700    Figure 1—figure supplement 2—Source Data 1

701    Figure 1—figure supplement 3—Source Data 1

702    Figure 1—figure supplement 4—Source Data 1

703    Figure 2—figure supplement 1—Source Data 1

704    Figure 4—figure supplement 1—Source Data 1

705    Figure 4—figure supplement 2—Source Data 1

706    Figure 4—figure supplement 3—Source Data 1

707    Figure 4—figure supplement 4—Source Data 1

708    Figure 4—figure supplement 5—Source Data 1

709    Figure 5—figure supplement 1—Source Data 1

710    Figure 5—figure supplement 2—Source Data 1

711     Figure 6—figure supplement 1—Source Data 1

712     Figure 6—figure supplement 2—Source Data 1

713

714     **<u>Supplementary Files</u>**

715     Supplementary file 1

716     **References**

717     **Mammalian iron metabolism and its control by iron regulatory proteins** CP Anderson, M

718     Shen, RS Eisenstein, EA Leibold (2012) *Biochimica et Biophysica Acta* **1823**:1468-1483. doi:

719     10.1016/j.bbamcr.2012.05.010

720     **Iron Homeostasis** NC Andrews, PJ Schmidt (2007) *Annual Review of Physiology* **69**:69-85.

721     https//doi.org/10.1146/annurev.physiol.69.031905.164337

722     **Ferric carboxymaltose in patients with heart failure and iron deficiency** SD Anker, J

723     Comin Colet, G Filippatos, R Willenheimer, K Dickstein, H Drexler, TF Lüscher, B Bart, W

724     Banasiak, J Niegowska, BA Kirwan, C Mori, B von Eisenhart Rothe, SJ Pocock, PA Poole-

725     Wilson, P Ponikowski (2009) *New England Journal of Medicine* **361**:2436-2448.

726     https//doi.org/10.1056/NEJMoa0908355

727     **Ferritins: A family of molecules for iron storage, antioxidation and more** P Arosio, R

728     Ingrassia, P Cavadini (2009) *Biochimica et Biophysica Acta (BBA) - General Subjects*

729     **1790**:589-599. https//doi.org/10.1016/j.bbagen.2008.09.004

730     **Lipid peroxidation: production, metabolism, and signaling mechanisms of**

731     **malondialdehyde and 4-hydroxy-2-nonenal** A Ayala, MF Muñoz, S Argüelles (2014)

732     *Oxidative Medicine and Cellular Longevity* **2014**:360438-360438.

733     https//doi.org/10.1155/2014/360438

734     **NCOA4 deficiency impairs systemic iron homeostasis** R Bellelli, G Federico, A Matte, D

735     Colecchia, A Iolascon, M Chiariello, M Santoro, L De Franceschi, F Carlomagno (2016) *Cell*

736     *Reports* **14**:411-421. https//doi.org/10.1016/j.celrep.2015.12.065

737     **Ferroptosis: an iron-dependent form of nonapoptotic cell death** SJ Dixon, KM Lemberg,

738     MR Lamprecht, R Skouta, EM Zaitsev, CE Gleason, DN Patel, AJ Bauer, AM Cantley, WS

739     Yang, B Morrison, 3rd, BR Stockwell (2012) *Cell* **149**:1060-1072.

740     https//doi.org/10.1016/j.cell.2012.03.042

**Selective VPS34 inhibitor blocks autophagy and uncovers a role for NCOA4 in ferritin degradation and iron homeostasis in vivo** WE Dowdle, B Nyfeler, J Nagel, RA Elling, S Liu, E Triantafellow, S Menon, Z Wang, A Honda, G Pardee, J Cantwell, C Luu, I Cornella-Taracido, E Harrington, P Fekkes, H Lei, Q Fang, ME Digan, D Burdick, AF Powers, SB Helliwell, S D'Aquin, J Bastien, H Wang, D Wiederschain, J Kuerth, P Bergman, D Schwalb, J Thomas, S Ugwonali, F Harbinski, J Tallarico, CJ Wilson, VE Myer, JA Porter, DE Bussiere, PM Finan, MA Labow, X Mao, LG Hamann, BD Manning, RA Valdez, T Nicholson, M Schirle, MS Knapp, EP Keaney, LO Murphy (2014) *Nature Cell Biology* **16**:1069-1079. https//doi.org/10.1038/ncb3053

**Loss of Cardiac Ferritin H Facilitates Cardiomyopathy via Slc7a11-Mediated Ferroptosis** X Fang, Z Cai, H Wang, D Han, Q Cheng, P Zhang, F Gao, Y Yu, Z Song, Q Wu, P An, S Huang, J Pan, HZ Chen, J Chen, A Linkermann, J Min, F Wang (2020) *Circulation Research* **127**:486-501. https//doi.org/10.1161/CIRCRESAHA.120.316509

**Ferroptosis as a target for protection against cardiomyopathy** X Fang, H Wang, D Han, E Xie, X Yang, J Wei, S Gu, F Gao, N Zhu, X Yin, Q Cheng, P Zhang, W Dai, J Chen, F Yang, HT Yang, A Linkermann, W Gu, J Min, F Wang (2019) *Proceedings of the National Academy of Sciences of the United States of America* **116**:2672-2680. https//doi.org/10.1073/pnas.1821022116

**Inactivation of the ferroptosis regulator Gpx4 triggers acute renal failure in mice** JP Friedmann Angeli, M Schneider, B Proneth, YY Tyurina, VA Tyurin, VJ Hammond, N Herbach, M Aichler, A Walch, E Eggenhofer, D Basavarajappa, O Radmark, S Kobayashi, T Seibt, H Beck, F Neff, I Esposito, R Wanke, H Forster, O Yefremova, M Heinrichmeyer, GW Bornkamm, EK Geissler, SB Thomas, BR Stockwell, VB O'Donnell, VE Kagan, JA Schick, M Conrad (2014) *Nature Cell Biology* **16**:1180-1191. https//doi.org/10.1038/ncb3064

765 **Iron supply via NCOA4-mediated ferritin degradation maintains mitochondrial**

766 **functions** M Fujimaki, N Furuya, S Saiki, T Amo, Y Imamichi, N Hattori (2019) *Molecular*

767 *and Cellular Biology*. https//doi.org/10.1128/MCB.00010-19

768 **Glutaminolysis and transferrin regulate ferroptosis** M Gao, P Monian, N Quadri, R

769 Ramasamy, X Jiang (2015) *Molecular Cell* **59**:298-308.

770 https//doi.org/10.1016/j.molcel.2015.06.011

771 **Iron and heart failure: Diagnosis, therapies, and future directions** K Ghafourian, JS

772 Shapiro, L Goodman, H Ardehali (2020) *JACC: Basic to Translational Science* **5**:300-313.

773 https//doi.org/10.1016/j.jacbts.2019.08.009

774 **Iron-regulatory proteins secure iron availability in cardiomyocytes to prevent heart**

775 **failure** S Haddad, Y Wang, B Galy, M Korf-Klingebiel, V Hirsch, AM Baru, F Rostami, MR

776 Reboll, J Heineke, U Flögel, S Groos, A Renner, K Toischer, F Zimmermann, S Engeli, J

777 Jordan, J Bauersachs, MW Hentze, KC Wollert, T Kempf (2016) *European Heart Journal*

778 **38**:362-372. https//doi.org/10.1093/eurheartj/ehw333

779 **Circulating interleukin-6 family cytokines and their receptors in patients with congestive**

780 **heart failure** H Hirota, M Izumi, T Haraguchi, S Sugiyama, E Murakami, K Kunisada, Y

781 Fujio, Y Oshima, Y Nakaoka, K Yamauchi-Takihara (2004) *Heart Vessels* **19**:237–241.

782 https://doi.org/10.1007/s00380-004-0770-z

783 **Serum ferritin is an important inflammatory disease marker, as it is mainly a leakage**

784 **product from damaged cells** DB Kell, Pretorius E (2014) *Metallomics* 2014 **6**:748-773.

785 https//doi.org/10.1039/c3mt00347g

786 **Iron deficiency in heart failure: getting to the guidelines** AJ Lavoie (2020) *Current Opinion*

787 *in Cardiology* **35**:133-137. https//doi.org/10.1097/hco.0000000000000714

788 **Ferroptosis: past, present and future** J Li, F Cao, H-I Yin, Z-J Hung, Z-T Lin, N Mao, G

789 Wang (2020) *Cell Death and Disease* **11**:88. https://doi.org/10.1038/s41419-020-2298-2.

**Synchronized renal tubular cell death involves ferroptosis** A Linkermann, R Skouta, N Himmerkus, SR Mulay, C Dewitz, F De Zen, A Prokai, G Zuchtriegel, F Krombach, P-S Welz, R Weinlich, T Vanden Berghe, P Vandenabeele, M Pasparakis, M Bleich, JM Weinberg, CA Reichel, JH Bräsen, U Kunzendorf, H-J Anders, BR Stockwell, DR Green, S Krautwald (2014) *Proceedings of the National Academy of Sciences* **111**:16836-16841. https//doi.org/10.1073/pnas.1415518111

**Quantitative proteomics identifies NCOA4 as the cargo receptor mediating ferritinophagy** JD Mancias, X Wang, SP Gygi, JW Harper, AC Kimmelman (2014) *Nature* **509**:105-109. https//doi.org/10.1038/nature13148

**The transport of glutamine into mammalian cells** JD McGivan, CI Bungard (2007) *Frontiers in Bioscience* **12**:874-882. https//doi.org/10.2741/2109

**Insight into the mechanism of ferroptosis inhibition by ferrostatin-1** G Miotto, M Rossetto, ML Di Paolo, L Orian, R Venerando, A Roveri, AM Vuckovic, V Bosello Travain, M Zaccarin, L Zennaro, M Maiorino, S Toppo, F Ursini, G Cozza (2020) *Redox Biology* **28**:101328. https//doi.org/10.1016/j.redox.2019.101328

**FKBP8 protects the heart from hemodynamic stress by preventing the accumulation of misfolded proteins and endoplasmic reticulum-associated apoptosis in mice** T Misaka, T Murakawa, K Nishida, Y Omori, M Taneike, S Omiya, C Molenaar, Y Uno, O Yamaguchi, J Takeda, AM Shah, K Otsu (2018) *Journal of Molecular and Cellular Cardiology* **114**:93-104. https//doi.org/10.1016/j.yjmcc.2017.11.004

**p38alpha mitogen-activated protein kinase plays a critical role in cardiomyocyte survival but not in cardiac hypertrophic growth in response to pressure overload** K Nishida, O Yamaguchi, S Hirotani, S Hikoso, Y Higuchi, T Watanabe, T Takeda, S Osuka, T Morita, G Kondoh, Y Uno, K Kashiwase, M Taniike, A Nakai, Y Matsumura, J Miyazaki, T Sudo, K

Hongo, Y Kusakari, S Kurihara, KR Chien, J Takeda, M Hori, K Otsu (2004) *Molecular and Cellular Biology* **24**:10611-10620. https//doi.org/10.1128/MCB.24.24.10611-10620.2004

**Mitochondrial DNA that escapes from autophagy causes inflammation and heart failure** T Oka, S Hikoso, O Yamaguchi, M Taneike, T Takeda, T Tamai, J Oyabu, T Murakawa, H Nakayama, K Nishida, S Akira, A Yamamoto, I Komuro, K Otsu (2012) *Nature* **485**:251-255. https//doi.org/10.1038/nature10992

**Downregulation of ferritin heavy chain increases labile iron pool, oxidative stress and cell death in cardiomyocytes** S Omiya, S Hikoso, Y Imanishi, A Saito, O Yamaguchi, T Takeda, I Mizote, T Oka, M Taneike, Y Nakano, Y Matsumura, K Nishida, Y Sawa, M Hori, K Otsu (2009) *Journal of Molecular and Cellular Cardiology* **46**:59-66. https//doi.org/10.1016/j.yjmcc.2008.09.714

**Cytokine mRNA degradation in cardiomyocytes restrains sterile inflammation in pressure-overloaded hearts** S Omiya, Y Omori, M Taneike, T Murakawa, J Ito, Y Tanada, K Nishida, O Yamaguchi, T Satoh, AM Shah, S Akira, K Otsu (2020) *Circulation* **141**:667-677. https//doi.org/10.1161/CIRCULATIONAHA.119.044582

**Basic mechanisms of oxidative stress and reactive oxygen species in cardiovascular injury** CA Papaharalambus, KK Griendling (2007) *Trends in Cardiovascular Medicine* **17**:48-54. https//doi.org/10.1016/j.tcm.2006.11.005

**Iron metabolism and toxicity** G Papanikolaou, K Pantopoulos (2005) *Toxicology and Applied Pharmacology* **202**:199-211. https//doi.org/10.1016/j.taap.2004.06.021

**2016 ESC Guidelines for the diagnosis and treatment of acute and chronic heart failure: The Task Force for the diagnosis and treatment of acute and chronic heart failure of the European Society of Cardiology (ESC)Developed with the special contribution of the Heart Failure Association (HFA) of the ESC** P Ponikowski, AA Voors, SD Anker, H Bueno, JGF Cleland, AJS Coats, V Falk, JR González-Juanatey, V-P Harjola, EA Jankowska, M

Jessup, C Linde, P Nihoyannopoulos, JT Parissis, B Pieske, JP Riley, GMC Rosano, LM Ruilope, F Ruschitzka, FH Rutten, P van der Meer, ESD Group (2016) *European Heart Journal* **37**:2129-2200. https//doi.org/10.1093/eurheartj/ehw128

**Increased heme levels in the heart lead to exacerbated ischemic injury** KT Sawicki, M Shang, R Wu, HC Chang, A Khechaduri, T Sato, C Kamide, T Liu, SVN Prasad, H Ardehali (2015) *Journal of the American Heart Association* **4**:e002272. https//doi.org/doi:10.1161/JAHA.115.002272

**In search of new therapeutic targets and strategies for heart failure: recent advances in basic science** AM Shah, DL Mann (2011) *Lancet* **378**:704-712. https//doi.org/10.1016/s0140-6736(11)60894-5

**Ferrostatins inhibit oxidative lipid damage and cell death in diverse disease models** R Skouta, SJ Dixon, J Wang, DE Dunn, M Orman, K Shimada, PA Rosenberg, DC Lo, JM Weinberg, A Linkermann, BR Stockwell (2014) *Journal of the American Chemical Society* **136**:4551-4556. https//doi.org/10.1021/ja411006a

**Tau-mediated iron export prevents ferroptotic damage after ischemic stroke** QZ Tuo, P Lei, KA Jackman, XL Li, H Xiong, XL Li, ZY Liuyang, L Roisman, ST Zhang, S Ayton, Q Wang, PJ Crouch, K Ganio, XC Wang, L Pei, PA Adlard, YM Lu, R Cappai, JZ Wang, R Liu, AI Bush (2017) *Molecular Psychiatry* **22**:1520-1530. https//doi.org/10.1038/mp.2017.171

**Cell death in the pathogenesis of heart disease: Mechanisms and significance** RS Whelan, V Kaplinskiy, RN Kitsis (2010) *Annual Review of Physiology* **72**:19-44. https//doi.org/10.1146/annurev.physiol.010908.163111

**Regulation of ferroptotic cancer cell death by GPX4** WS Yang, R SriRamaratnam, ME Welsch, K Shimada, R Skouta, VS Viswanathan, JH Cheah, PA Clemons, AF Shamji, CB Clish, LM Brown, AW Girotti, VW Cornish, SL Schreiber, BR Stockwell (2014) *Cell* **156**:317-331. https//doi.org/10.1016/j.cell.2013.12.010

864    **Involvement of cigarette smoke-induced epithelial cell ferroptosis in COPD pathogenesis**

865    M Yoshida, S Minagawa, J Araya, T Sakamoto, H Hara, K Tsubouchi, Y Hosaka, A Ichikawa,

866    N Saito, T Kadota, N Sato, Y Kurita, K Kobayashi, S Ito, H Utsumi, H Wakui, T Numata, Y

867    Kaneko, S Mori, H Asano, M Yamashita, M Odaka, T Morikawa, K Nakayama, T Iwamoto,

868    H Imai, K Kuwano (2019) *Nature Communications* **10**:3145. https//doi.org/10.1038/s41467-

869    019-10991-7

870

**Figures legends**

**Figure 1. Cardiomyocyte-specific *Ncoa4* ablation attenuated the development of pressure**

**overload-induced heart failure**. The *Ncoa4*$^{+/+}$ and *Ncoa4*$^{-/-}$ mice were subjected to pressure

overload by transverse aortic constriction (TAC) and analyzed 4 weeks after the operation. (**A**)

Representative images of transthoracic M-mode echocardiographic tracing. Scale bars, 0.1 s

and 2 mm, respectively. (**B**) Echocardiographic parameters of the mice (*n* =10 biologically

independent samples). LVIDd and LVIDs, end-diastolic and end-systolic left ventricular (LV)

internal dimensions; IVSd, end-diastolic interventricular septum thickness; LVPWd, end-

diastolic LV posterior wall thickness; FS, fractional shortening. (**C**) Physiological parameters

of the mice (*n* = 10 biologically independent samples). (**D**) Representative images of the

hematoxylin-eosin-stained (upper), Masson's trichrome-stained (middle), and wheat germ

agglutinin-stained (lower) heart sections. Scale bar, 50 μm. The upper and lower right graphs

show the ratio of the fibrotic area to whole heart section and the cross-sectional area of

cardiomyocytes, respectively (*n* = 5 biologically independent samples). The data were

evaluated by one-way analysis of variance (ANOVA), followed by Tukey–Kramer's post hoc

test. $^{*}P$ < 0.05, $^{**}P$ < 0.001, $^{***}P$ < 0.0001. NS, *P* > 0.05. Exact *P* values are provided in

Supplementary file 1. Source Data file is provided for Figure 1B, C, and D.

**Figure 2. The time course of ferritinophagy in the heart after TAC**. (**A**) Western blot

analysis of FTH1 in *Ncoa4*$^{+/+}$ and *Ncoa4*$^{-/-}$ hearts 4 weeks after TAC. GAPDH was used as the

loading control. The right-hand graphs show the densitometric analysis. The average value for

sham-operated *Ncoa4*$^{+/+}$ hearts was set to 1 (biologically independent samples: *n* = 6). (**B**)

mRNA expression of *Fth1* in the heart 4 weeks after TAC. *Gapdh* mRNA was used as the

loading control. The average value for sham-operated *Ncoa4*$^{+/+}$ hearts was set to 1 (biologically

896    independent samples: $n = 8$). (**C** through **H**) The $Ncoa4^{+/+}$ mice were subjected to TAC and

897    analyzed 3 days after sham operation and 3, 5, and 7 days and 4 weeks after the operation. (**C**)

898    Heart homogenates after TAC were subjected to Western blot analysis using anti-FTH1

899    antibody ($n = 5$ biologically independent samples for each group). GAPDH was used as the

900    loading control. (**D**) Cardiac *Fth1* mRNA levels after TAC ($n = 5$ biologically independent

901    samples). *Gapdh* mRNA was used as the loading control. (**E** and **F**) Immunofluorescence

902    analysis of LC3B (green) and FTH1 (red) in the heart after TAC ($n = 5$ biologically independent

903    samples). (**G** and **H**) Immunofluorescence analysis of LAMP2a (green) and FTH1 (red) in the

904    heart after TAC ($n = 5$ biologically independent samples). Scale bar, 5 μm in (**E**) and (**G**).

905    Arrows indicate double-positive dots. The values are presented as the mean ± SEM. The data

906    were evaluated by one-way analysis of variance (ANOVA), followed by Tukey–Kramer's post

907    hoc test. $^*P < 0.05$, $^{**}P < 0.001$, $^{***}P < 0.0001$. NS, $P > 0.05$ versus sham-operated group. Exact

908    *P* values are provided in Supplementary file 1. Source Data file is provided for Figure 2A, B,

909    C, D, F, and H.

910

911    **Figure 3. Ablation of *Ncoa4* in cardiomyocytes showed defective ferritinophagy**. (**A**)

912    Western blot analysis of FTH1 in $Ncoa4^{+/+}$ and $Ncoa4^{-/-}$ hearts 1 week after TAC. GAPDH

913    was used as the loading control. The right-hand graphs show the densitometric analysis. The

914    average value for sham-operated $Ncoa4^{+/+}$ hearts was set to 1 (biologically independent

915    samples: $n = 5$). (**B**) mRNA expression of *Fth1* in the heart 1 week after TAC. *Gapdh* mRNA

916    was used as the loading control. The average value for sham-operated $Ncoa4^{+/+}$ hearts was set

917    to 1 (biologically independent samples: $n = 5$). (**C** and **D**) Immunofluorescence analysis of

918    LC3B (green) and FTH1 (red) in the heart 1 week after TAC. The number of LC3B- and FTH1-

919    positive dots are shown in (**D**). (**E** and **F**) Immunofluorescence analysis of LAMP2a (green)

920    and FTH1 (red) in the heart 1 week after TAC. The number of LAPM2a- and FTH1-positive

921     dots are shown in (**F**). In (**C**) and (**E**), images of the square in the merged images are shown at

922     higher magnification in the right three columns. Scale bar, 5 μm. Arrows indicate double-

923     positive dots. The data were evaluated by one-way analysis of variance (ANOVA), followed

924     by Tukey–Kramer's post hoc test. $^*P < 0.05$, $^{**}P < 0.001$, $^{***}P < 0.0001$. NS, $P > 0.05$. Exact

925     *P* values are provided in Supplementary file 1. Source Data file is provided for Figure 3A, B,

926     C, D, and F.

927

928     **Figure 4. The effect of *Ncoa4* ablation on the pathways to iron-dependent cell death**. (**A**)

929     Tissue levels of total non-heme, ferrous, and ferric iron in $Ncoa4^{+/+}$ and $Ncoa4^{-/-}$ hearts 4 weeks

930     after TAC ($n = 6$ biologically independent samples). The ratio of the ferrous iron level to the

931     FTH1 protein level is shown in the right-most panel. The FTH1 protein level for sham-operated

932     $Ncoa4^{+/+}$ estimated as Western blot analysis in hearts was set to 1. (**B**) Malondialdehyde (MDA)

933     levels in heart homogenates ($n = 5$ biologically independent samples). (**C**) *Ptgs2* mRNA levels

934     in the heart ($n = 8$ biologically independent samples). (**D**) Serum troponin T (TnT) levels ($n =$

935     8 biologically independent samples). (**E**) Glutathione peroxidase 4 (GPX4) levels in the heart

936     homogenates. The right panel shows the ratio of GPX4 to GAPDH ($n = 6$ biologically

937     independent samples). (**F**) The levels of total glutathione (GSH+GSSG), reduced (GSH) and

938     oxidized (GSSG) glutathione and the ratio of GSH to GSSG in heart homogenates ($n = 5$

939     biologically independent samples). GSH levels were calculated by subtracting GSSG from total

940     glutathione. (**G**) Cardiac glutamine levels ($n = 5$ biologically independent samples). The data

941     were evaluated by one-way analysis of variance (ANOVA), followed by Tukey–Kramer's post

942     hoc test. $^*P < 0.05$, $^{**}P < 0.001$, $^{***}P < 0.0001$. NS, $P > 0.05$. Exact *P* values are provided in

943     Supplementary file 1. Source Data file is provided for Figure 4A, B, C, D, E, F, and G.

944

945 **Figure 5. Isoproterenol induces iron-dependent cell death in isolated cardiomyocytes**. (**A**)

946 Cell death assay. Cell death was estimated using a Live/Dead Viability/Cytotoxicity Assay Kit.

947 Isolated mouse cardiomyocytes from $Ncoa4^{+/+}$ and $Ncoa4^{-/-}$ hearts were treated with the

948 indicated concentrations of isoproterenol (Iso) with or without ferrostatin-1 (Fer-1) for 4 hours.

949 Calcein-AM (green) is retained in live cells, while ethidium homodimer produces red

950 fluorescence in dead cells. Scale bar, 100 μm. The percentage of dead cells is shown in the

951 middle left-hand graphs ($n = 5$ biologically independent samples). (**B** and **C**) The accumulation

952 of cellular (**B**) and lipid (**C**) reactive oxygen species (ROS) were assessed by H2DCFDA and

953 C11-BODIPY, respectively ($n = 5$ biologically independent samples). (**D**) The labile iron pool

954 was measured using the calcein-AM method in isolated mouse cardiomyocytes ($n = 5$

955 biologically independent samples). (E) Western blot analysis of FTH1 in isolated mouse

956 cardiomyocytes from $Ncoa4^{+/+}$ and $Ncoa4^{-/-}$ hearts. GAPDH was used as the loading control.

957 The right-hand graphs show the densitometric analysis ($n = 5$ biologically independent

958 samples). The average value for vehicle-treated without ferrostatin-1 $Ncoa4^{+/+}$ cardiomyocytes

959 was set to 1. The values are presented as the mean ± SEM. Two-way analysis of variance

960 (ANOVA) followed by Tukey's multiple comparisons test was used. $^{*}P < 0.05$, $^{**}P < 0.001$,

961 $^{***}P < 0.0001$. NS, $P > 0.05$ versus $Ncoa4^{+/+}$ control without ferrostatin-1 treatment. $^{†}P < 0.05$,

962 $^{††}P < 0.001$, $^{†††}P < 0.0001$. NS, $P > 0.05$ versus the corresponding group without ferrostatin-1

963 treatment. $^{‡}P < 0.05$, $^{‡‡}P < 0.001$, $^{‡‡‡}P < 0.0001$. NS, $P > 0.05$ versus the corresponding

964 $Ncoa4^{+/+}$. Exact $P$ values are provided in Supplementary file 1. Source Data file is provided

965 for Figure 5A, B, C, D, and E.

966

967 **Figure 6. Inhibition of lipid peroxidation protects hearts from pressure overload**. Wild-

968 type C57BL/6J mice were subjected to TAC and analyzed 4 weeks after the operation.

969 Ferrostatin-1 (Fer-1) or saline was intraperitoneally administered daily starting 1 day before

970  TAC. **(A)** Representative images of transthoracic M-mode echocardiographic tracing. Scale

971  bars, 0.1 s and 2 mm, respectively. **(B)** Echocardiographic parameters of the mice ($n = 10$

972  biologically independent samples). **(C)** Physiological parameters of the mice ($n = 10$

973  biologically independent samples). **(D)** Histological analysis of the heart. Scale bar, 50 μm.

974  The upper and lower right graphs show the ratio of the fibrotic area to whole heart section and

975  the cross-sectional area of cardiomyocytes, respectively ($n = 5$ biologically independent

976  samples). **(E)** Cardiac MDA levels ($n = 5$ biologically independent samples). **(F)** *Ptgs2* mRNA

977  levels in the hearts ($n = 8$ biologically independent samples). The data were evaluated by one-

978  way analysis of variance (ANOVA) followed by Tukey–Kramer's post hoc test. $^{*}P < 0.05$, $^{**}P$

979  $< 0.001$, $^{***}P < 0.0001$. NS, $P > 0.05$. Exact $P$ values are provided in Supplementary file 1.

980  Source Data file is provided for Figure 6B, C, D, E, and F.

981

982  **Figure 1—figure supplement 1. Generation of cardiomyocyte-specific NCOA4-deficient**

983  **mice**. **(A)** Targeted modification of the *Ncoa4* gene. Schematic structures of the wild-type

984  genomic *Ncoa4* sequence, the targeting construct, the targeted allele, the floxed allele after

985  flippase recognition target site (*FRT*)-mediated *neomycin*-resistance gene (*Neo*) deletion, and

986  the deleted allele after Cre-mediated recombination are indicated from *top* to *bottom*. The *black*

987  and *white arrowheads* indicate *loxP* and *FRT* sites, respectively. The *neomycin* resistance gene

988  (*PGK-Neo* cassette) was inserted between exon 6 and the downstream *loxP* site. The diphtheria

989  toxin A (*DT*) gene was positioned at the 3' end of the targeting construct for negative selection.

990  The *bar* labelled as "probe" corresponds to the sequence used for Southern blotting. The scale

991  bar indicates 2 kbp. **(B)** Genomic analysis of embryonic stem (ES) cells. To identify

992  homologous recombinants, genomic DNA extracted from ES cells was digested with EcoRV

993  and analyzed by Southern blotting with the 5' and 3' probe, respectively. Wild-type and

994  targeted allele respectively showed 7,748 and 6,172 bp using the 5' probe (left) and 5,269 and

995  6,924 bp using the 3' probe (right). The ES cells with *Ncoa4*-floxed allele were injected into

996  blastocysts to obtain *Ncoa4*^flox/+ mice. (**C**) Protein expression levels of NCOA4 in *Ncoa4*^+/+ and

997  *Ncoa4*^−/− hearts. Left ventricular homogenates from *Ncoa4*^+/+ and *Ncoa4*^−/− mice were

998  immunoprecipitated with anti-NCOA4 antibody, followed by Western blotting with the

999  antibody. Densitometric analysis is shown. (**D**) mRNA expression levels of *Ncoa4*. The

1000  average value of NCOA4 (C) or *Ncoa4*-to-*Gapdh* ratio (D) in *Ncoa4*^+/+ was set equal to 1. The

1001  values are presented as the mean ± SEM of 4 mice for protein expression and 8 mice for mRNA

1002  expression in each group. The data were evaluated by unpaired, two-tailed Student's *t*-test.

1003  Source Data file is provided for Figure 1—figure supplement 1C and D.

1004

1005  **Figure 1—figure supplement 2. Physiological and echocardiographic parameters in 8- to**

1006  **10-week-old *Ncoa4*^+/+ and *Ncoa4*^−/− mice at baseline.** BP, blood pressure; TL, tibia length;

1007  LV, left ventricle; LVIDd, end-diastolic left ventricular internal dimension; LVIDs, end-

1008  systolic left ventricular internal dimension; IVSd, end-diastolic interventricular septum

1009  thickness; LVPWd, end-diastolic left ventricular posterior wall thickness; FS, fractional

1010  shortening. The data are the mean ± SEM. *n* indicates the number of biologically independent

1011  samples. The data were evaluated by unpaired, two-tailed Student's *t*-test. Source Data file is

1012  provided for Figure 1—figure supplement 2.

1013

1014  **Figure 1—figure supplement 3. Cardiac remodeling markers in TAC-operated *Ncoa4*^−/−**

1015  **mice**. The *Ncoa4*^+/+ and *Ncoa4*^−/− mice were subjected to TAC. The levels of mRNA were

1016  analyzed 4 weeks after the operation (*n* = 8 biologically independent samples). *Gapdh* mRNA

1017  was used as the loading control. The values are presented as the mean ± SEM. The data were

1018  evaluated by one-way analysis of variance (ANOVA), followed by Tukey–Kramer's post hoc

1019    test. $^*P < 0.05$, $^{**}P < 0.001$, $^{***}P < 0.0001$. NS, $P > 0.05$. Exact $P$ values are provided in

1020    Supplementary file 1. Source Data file is provided for Figure 1—figure supplement 3.

1021

1022    **Figure 1—figure supplement 4. Myh6-Cre transgene does not alter the heart response to**

1023    **pressure overload stress**. The Myh6-Cre$^-$ and Myh6-Cre$^+$ mice were subjected to TAC and

1024    analyzed 4 weeks after the operation. Echocardiographic parameters of the mice ($n = 4$

1025    biologically independent samples) are shown. LVIDd and LVIDs, end-diastolic and end-

1026    systolic left ventricular (LV) internal dimensions; FS, fractional shortening. The values are

1027    presented as the mean ± SEM. The data were evaluated by unpaired, two-tailed Student's $t$-

1028    test. NS, $P > 0.05$. Exact $P$ values are provided in Supplementary file 1. Source Data file is

1029    provided for Figure 1—figure supplement 4.

1030

1031    **Figure 2—figure supplement 1. Echocardiographic parameter after TAC.** Time course of

1032    changes in the echocardiographic parameters of left ventricular (LV) fractional shortening

1033    (FS), the end-diastolic LV internal dimension (LVIDd) and the end-systolic LV internal

1034    dimension (LVIDs). Echocardiographic analysis on $Ncoa4^{+/+}$ and $Ncoa4^{-/-}$ mice were

1035    performed before (pre) and 3, 5, and 7 days after TAC (n = 3 biologically independent samples).

1036    The values are presented as the mean ± SEM. Two-way analysis of variance (ANOVA)

1037    followed by Tukey's multiple comparisons test was used. $^*P < 0.05$, $^{**}P < 0.001$, $^{***}P < 0.0001$.

1038    $P > 0.05$, sham-operated $Ncoa4^{+/+}$ versus TAC-operated $Ncoa4^{+/+}$. $^†P < 0.05$, $^{††}P < 0.001$, $^{†††}P$

1039    $< 0.0001$. $P > 0.05$, sham-operated $Ncoa4^{-/-}$ versus TAC-operated $Ncoa4^{-/-}$. $^‡P < 0.05$, $^{‡‡}P <$

1040    $0.001$, $^{‡‡‡}P < 0.0001$. $P > 0.05$, TAC-operated $Ncoa4^{+/+}$ versus TAC-operated $Ncoa4^{-/-}$. Exact

1041    $P$ values are provided in Supplementary file 1. Source Data file is provided for Figure 2—

1042    figure supplement 1.

1043

1044 **Figure 4—figure supplement 1. Hematological parameters and red cell indices in *Ncoa4*$^{+/+}$**

1045 **and *Ncoa4*$^{-/-}$ mice**. PCV, packed cell volume; MCV, mean corpuscular volume; MCH, mean

1046 corpuscular hemoglobin; MCHC, mean corpuscular hemoglobin concentration; CH,

1047 hemoglobin concentration. Data are the mean ± SEM. *n* indicates the number of biologically

1048 independent samples. The data were evaluated by one-way analysis of variance (ANOVA),

1049 followed by Tukey–Kramer's post hoc test. *$^*P$ = 0.0418 and $^{**}P$ = 0.0108 versus the

1050 corresponding sham-operated group. Exact *P* values are provided in Supplementary file 1.

1051 Source Data file is provided for Figure 4—figure supplement 1.

1052

1053 **Figure 4—figure supplement 2. Liver iron store and serum inflammatory cytokine in**

1054 ***Ncoa4*$^{+/+}$ and *Ncoa4*$^{-/-}$ mice**. (**A**) Tissue levels of total non-heme iron in *Ncoa4*$^{+/+}$ and *Ncoa4*$^{-}$

1055 $^{/-}$ livers 4 weeks after TAC (n = 6 biologically independent samples). (**B**) Serum interleukin 6

1056 (IL-6) levels (*n* = 8 biologically independent samples). The values are presented as the mean ±

1057 SEM. The data were evaluated by one-way analysis of variance (ANOVA), followed by

1058 Tukey–Kramer's post hoc test. *$^*P$ < 0.05, $^{**}P$ < 0.001, $^{***}P$ < 0.0001. NS, *P* > 0.05. Exact *P*

1059 values are provided in Supplementary file 1. Source Data file is provided for Figure 4—figure

1060 supplement 2A and B.

1061

1062 **Figure 4—figure supplement 3. Iron regulating proteins in TAC-operated *Ncoa4*$^{-/-}$**

1063 **hearts**. (**A**) Homogenates from the heart 4 weeks after TAC were subjected to Western blot

1064 analysis using antibodies against iron-responsive element-binding protein 2 (IREB2),

1065 ferroportin 1 (SLC40A1), and transferrin receptor 1 (TFRC) (*n* = 6 biologically independent

1066 samples). GAPDH was used as the loading control. (**B**) The levels of mRNA were analyzed 4

1067 weeks after the operation (*n* = 8 biologically independent samples). *Gapdh* mRNA was used

1068 as the loading control. (**C**) IRP activation in *Ncoa4*$^{+/+}$ and *Ncoa4*$^{-/-}$ hearts. The activation of

1069 IRP was analyzed by EMSA. Protein homogenates from mouse heart were incubated with the

1070 5' UTR of mouse *Slc40a1* containing IRE and subjected to electrophoresis. ($n = 3$ biologically

1071 independent samples). The values are presented as the mean ± SEM. The data were evaluated

1072 by one-way analysis of variance (ANOVA), followed by Tukey–Kramer's post hoc test. NS,

1073 $P > 0.05$. Exact $P$ values are provided in Supplementary file 1. Source Data file is provided for

1074 Figure 4—figure supplement 3A, B, and C.

1075

1076 **Figure 4—figure supplement 4. Lipid reactive oxygen species and anti-oxidant proteins**

1077 **in *Ncoa4*$^{-/-}$ hearts four weeks after TAC**. (**A**) 4-Hydroxy-2-noneal (HNE) staining of heart

1078 sections. Scale bar, 50 μm. The right panel shows the quantitative analysis of 4-HNE-positive

1079 area to whole heart section ($n = 5$ biologically independent samples). (**B**) Homogenates from

1080 the heart were subjected to Western blot analysis using antibodies against superoxide dismutase

1081 2 (SOD2) and heme oxygenase 1 (HO-1) ($n = 6$ biologically independent samples). GAPDH

1082 was used as the loading control. The values are presented as the mean ± SEM. The data were

1083 evaluated by one-way analysis of variance (ANOVA), followed by Tukey–Kramer's post hoc

1084 test. $^*P < 0.05$. NS, $P > 0.05$. Exact $P$ values are provided in Supplementary file 1. Source Data

1085 file is provided for Figure 4—figure supplement 4A and B.

1086

1087 **Figure 4—figure supplement 5. The system Xc$^-$/glutathione axis and glutaminolysis**

1088 **pathway in TAC-operated *Ncoa4*$^{-/-}$ hearts**. (**A**) The mRNA expression level of *Slc7a11* in

1089 the heart 4 weeks after TAC ($n = 8$ biologically independent samples). *Gapdh* mRNA was used

1090 as the loading control. (**B**) The cystine concentration in the heart was analyzed by high–

1091 performance liquid chromatography (HPLC) ($n = 4$ for sham-operated *Ncoa4*$^{+/+}$, $n = 5$ for TAC-

1092 operated *Ncoa4*$^{+/+}$, sham-operated *Ncoa4*$^{-/-}$, and TAC-operated *Ncoa4*$^{-/-}$ biologically

1093 independent samples). (**C**) Cardiac glutamate levels ($n = 5$ biologically independent samples).

48

1094 **(D)**The mRNA expression levels of *Slc38a1*, *Slc1a5*, *Slc7a5*, *Gls1,* and *Gls2* in the hearts 4

1095 weeks after TAC ($n$ = 8 biologically independent samples). *Gapdh* mRNA was used as the

1096 loading control. The values are presented as the mean ± SEM. The data were evaluated by one-

1097 way analysis of variance (ANOVA), followed by Tukey–Kramer's post hoc test. *$P$ < 0.05,

1098 ***$P$ < 0.0001. NS, $P$ > 0.05. Exact $P$ values are provided in Supplementary file 1. Source Data

1099 file is provided for Figure 4—figure supplement 5A, B, C, and D.

1100

1101 **Figure 5—figure supplement 1. Erasin induces cell death in isolated cardiomyocytes**. **(A)**

1102 Cell death assay. Cell death was estimated using a Live/Dead Viability/Cytotoxicity Assay Kit.

1103 Isolated mouse cardiomyocytes from *Ncoa4*$^{+/+}$ and *Ncoa4*$^{-/-}$ hearts were treated with the

1104 indicated concentrations of erastin (Era) with or without ferrostatin-1 (Fer-1) for 4 hours.

1105 Calcein-AM (green) is retained in live cells, while ethidium homodimer produces red

1106 fluorescence in dead cells. Scale bar, 100 μm. The percentage of dead cells is shown in the

1107 middle left-hand graphs ($n$ = 5 biologically independent samples). **(B** and **C)** The accumulation

1108 of cellular (B) and lipid (C) reactive oxygen species (ROS) were assessed by H2DCFDA and

1109 C11-BODIPY, respectively ($n$ = 5 biologically independent samples). **(D)** The labile iron pool

1110 was measured using the calcein-AM method in isolated mouse cardiomyocytes ($n$ = 5

1111 biologically independent samples). The average value for vehicle-treated without ferrostatin-1

1112 *Ncoa4*$^{+/+}$ cardiomyocytes was set to 1. The values are presented as the mean ± SEM. Two-way

1113 analysis of variance (ANOVA) followed by Tukey's multiple comparisons test was used. *$P$ <

1114 0.05, **$P$ < 0.001, ***$P$ < 0.0001. NS, $P$ > 0.05 versus *Ncoa4*$^{+/+}$ control without ferrostatin-1

1115 treatment. $^{†}P$ < 0.05, $^{††}P$ < 0.001, $^{†††}P$ < 0.0001. NS, $P$ > 0.05 versus the corresponding group

1116 without ferrostatin-1 treatment. $^{‡}P$ < 0.05, $^{‡‡}P$ < 0.001, $^{‡‡‡}P$ < 0.0001. NS, $P$ > 0.05 versus the

1117 corresponding *Ncoa4*$^{+/+}$. Exact $P$ values are provided in Supplementary file 1. Source Data file

1118 is provided for Figure 5—figure supplement 1A, B, C, and D.

1120 **Figure 5—figure supplement 2. RSL3 induces cell death in isolated cardiomyocytes**. Cell

1121 death assay. Cell death was estimated using a Live/Dead Viability/Cytotoxicity Assay Kit.

1122 Isolated mouse cardiomyocytes from *Ncoa4*<sup>+/+</sup> and *Ncoa4*<sup>−/−</sup> hearts were treated with the

1123 indicated concentrations of RSL3 with or without ferrostatin-1 (Fer-1) for 4 hours. Calcein-

1124 AM (green) is retained in live cells, while ethidium homodimer produces red fluorescence in

1125 dead cells. Scale bar, 100 μm. The percentage of dead cells is shown in the graphs ($n = 5$

1126 biologically independent samples). The values are presented as the mean ± SEM. Two-way

1127 analysis of variance (ANOVA) followed by Tukey's multiple comparisons test was used. $^*P <$

1128 0.05, $^{**}P < 0.001$, $^{***}P < 0.0001$. NS, $P > 0.05$ versus *Ncoa4*<sup>+/+</sup> control without ferrostatin-1

1129 treatment. $^†P < 0.05$, $^{††}P < 0.001$, $^{†††}P < 0.0001$. NS, $P > 0.05$ versus the corresponding group

1130 without ferrostatin-1 treatment. $^‡P < 0.05$, $^{‡‡}P < 0.001$, $^{‡‡‡}P < 0.0001$. NS, $P > 0.05$ versus the

1131 corresponding *Ncoa4*<sup>+/+</sup>. Exact $P$ values are provided in Supplementary file 1. Source Data file

1132 is provided for Figure 5—figure supplement 2.

1133

1134 **Figure 6—figure supplement 1**. **Cardiac remodeling markers and 4-HNE staining in**

1135 **ferrostatin-1-treated TAC-operated wild-type hearts**. The wild-type C57BL/6J mice were

1136 subjected to TAC. Ferrostatin-1 (Fer-1) was intraperitoneally administered daily starting one

1137 day before TAC. (**A**) The levels of mRNA were analyzed 4 weeks after the operation ($n = 8$

1138 biologically independent samples). *Gapdh* mRNA was used as the loading control. (**B**) 4-

1139 Hydroxy-2-noneal (4-HNE) staining of heart sections. Scale bar, 50 μm. The right panel shows

1140 the quantitative analysis of 4-HNE-positive area ($n = 5$ biologically independent samples). The

1141 values are presented as the mean ± SEM. The data were evaluated by one-way analysis of

1142 variance (ANOVA) followed by Tukey–Kramer's post hoc test. $^*P < 0.05$, $^{**}P < 0.001$, $^{***}P <$

1143     0.0001. NS, $P > 0.05$. Exact $P$ values are provided in Supplementary file 1. Source Data file is

1144     provided for Figure 6—figure supplement 1A and B.

1145

1146     **Figure 6—figure supplement 2**. **Ferrostatin-1 does not provide additional protection from**

1147     **cardiac remodeling in *Ncoa4$^{-/-}$* mice**. The *Ncoa4$^{-/-}$* mice were subjected to TAC. Ferrostatin-

1148     1 (Fer-1) or saline was intraperitoneally administered daily starting one day before TAC. (**A**)

1149     Echocardiographic parameters of the mice ($n = 5$ biologically independent samples). LVIDd

1150     and LVIDs, end-diastolic and end-systolic left ventricular (LV) internal dimensions; IVSd,

1151     end-diastolic interventricular septum thickness; LVPWd, end-diastolic LV posterior wall

1152     thickness; FS, fractional shortening. (**B**) Physiological parameters of the mice ($n = 5$

1153     biologically independent samples). The values are presented as the mean ± SEM. The data were

1154     evaluated by unpaired, two-tailed Student's $t$-test. NS, $P > 0.05$. Exact $P$ values are provided

1155     in Supplementary file 1. Source Data file is provided for Figure 6—figure supplement 2A and

1156     B.

1157

1158     **Supplementary file 1. Quantification and statistical analysis.** The number of independent

1159     biological repeats ($n$) is shown in the figure legends. $P$ values are shown below.
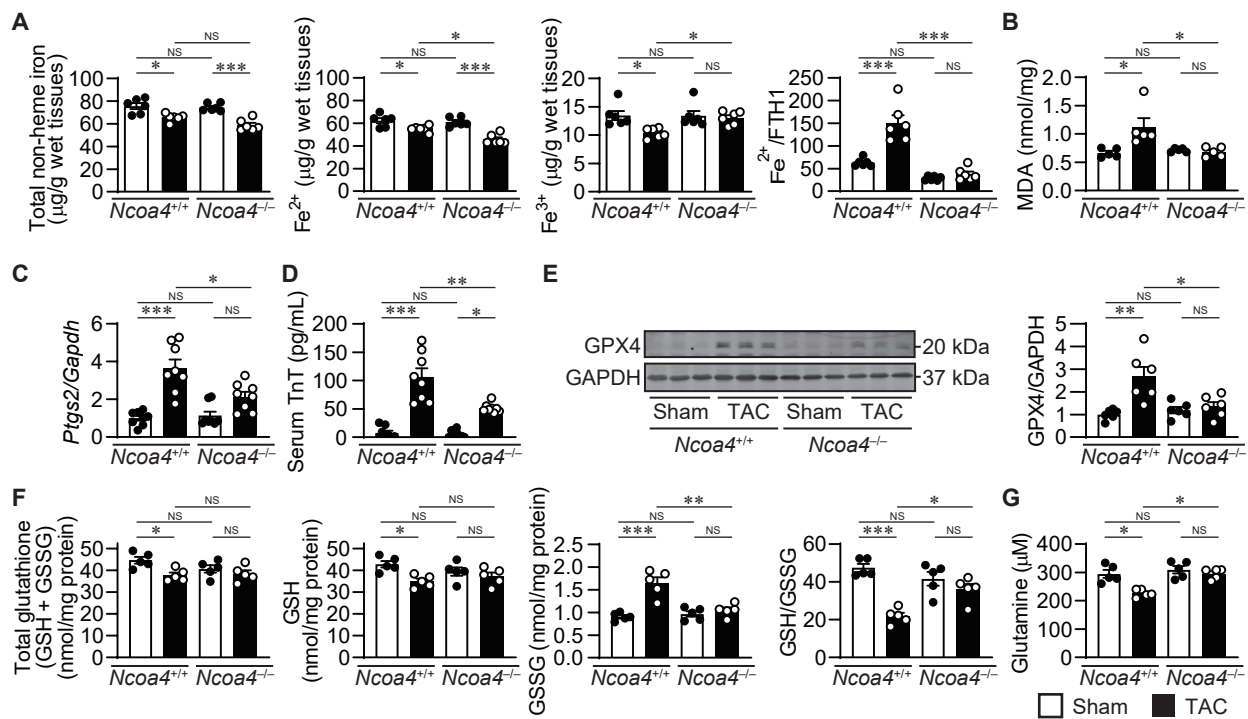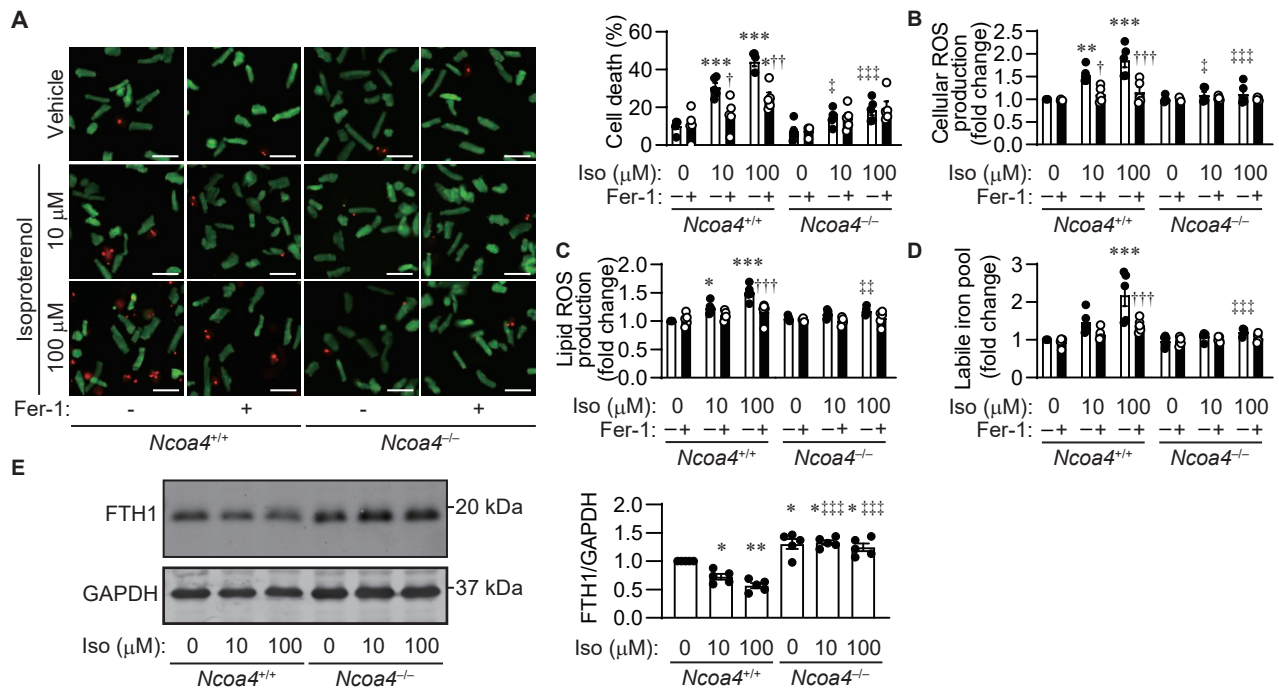
1160
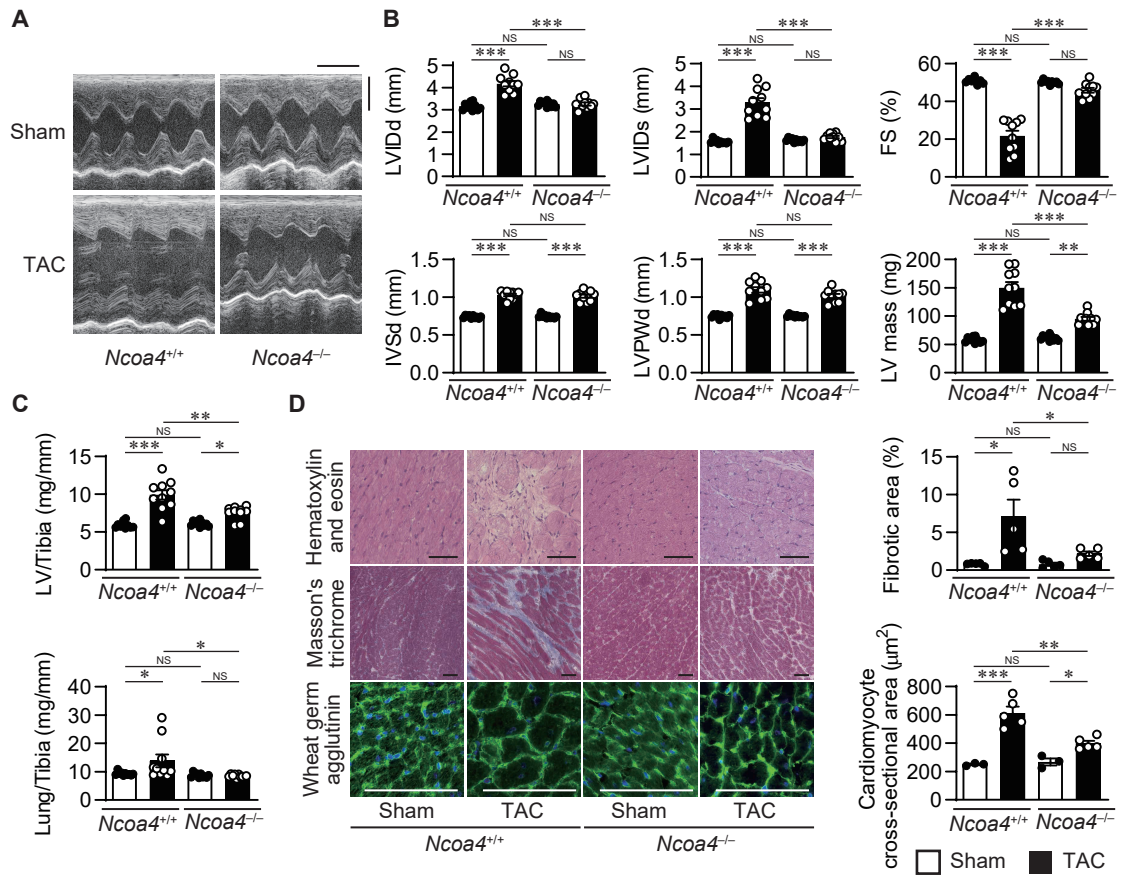
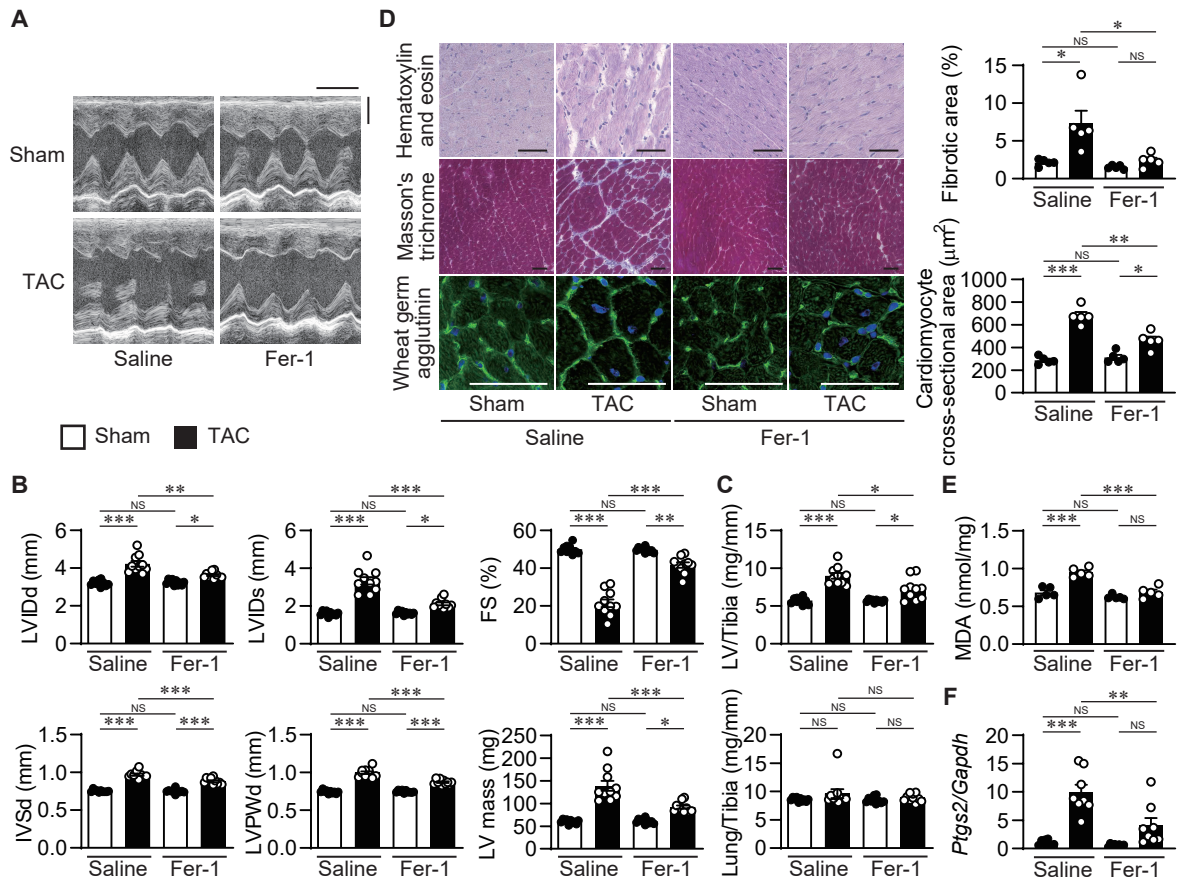Figure 1
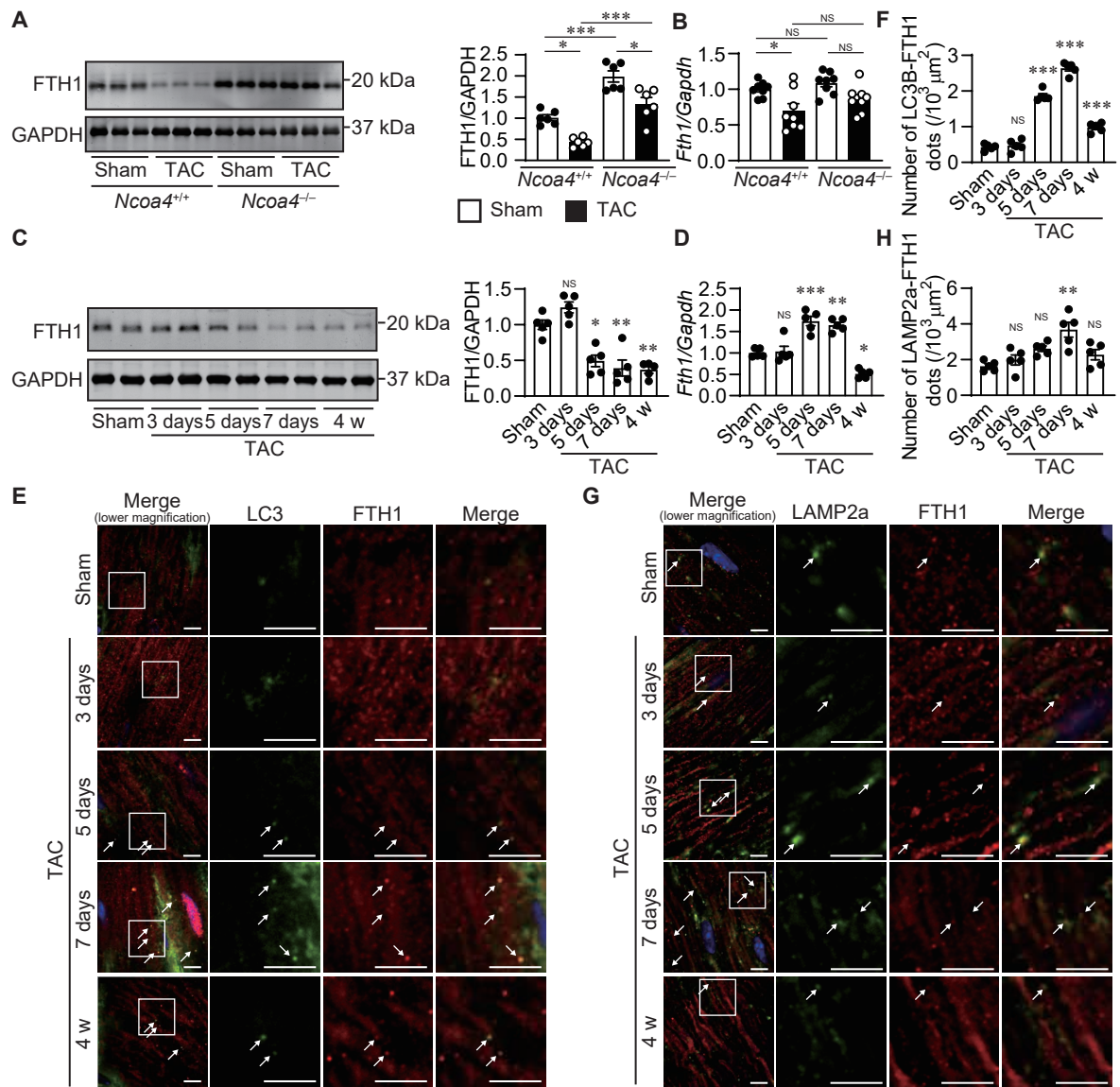
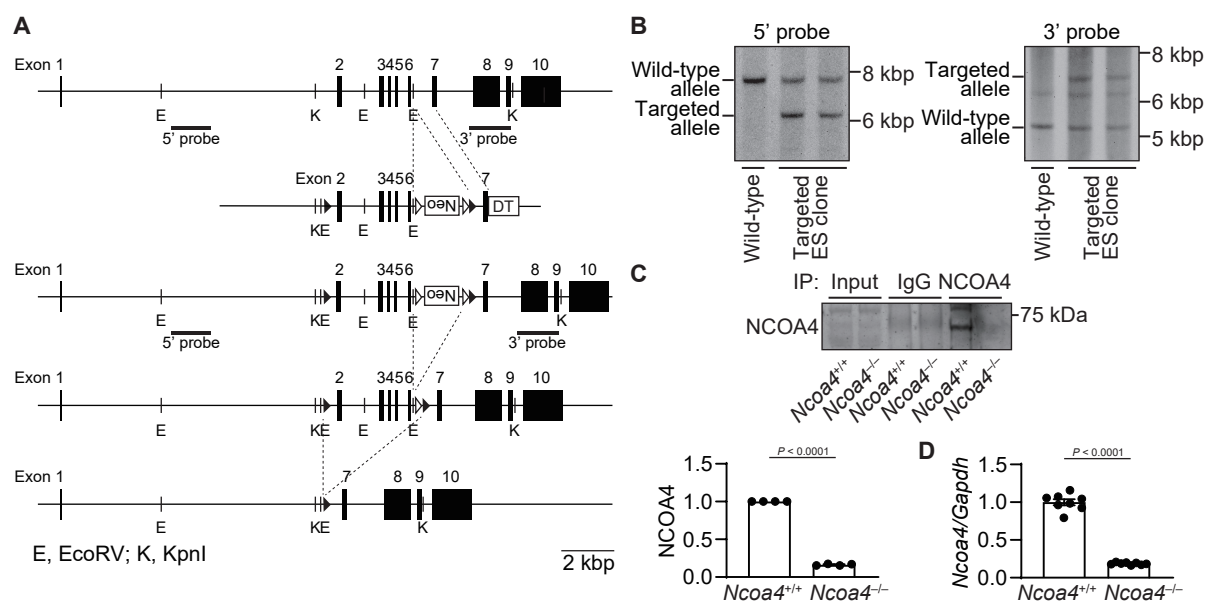Figure 2
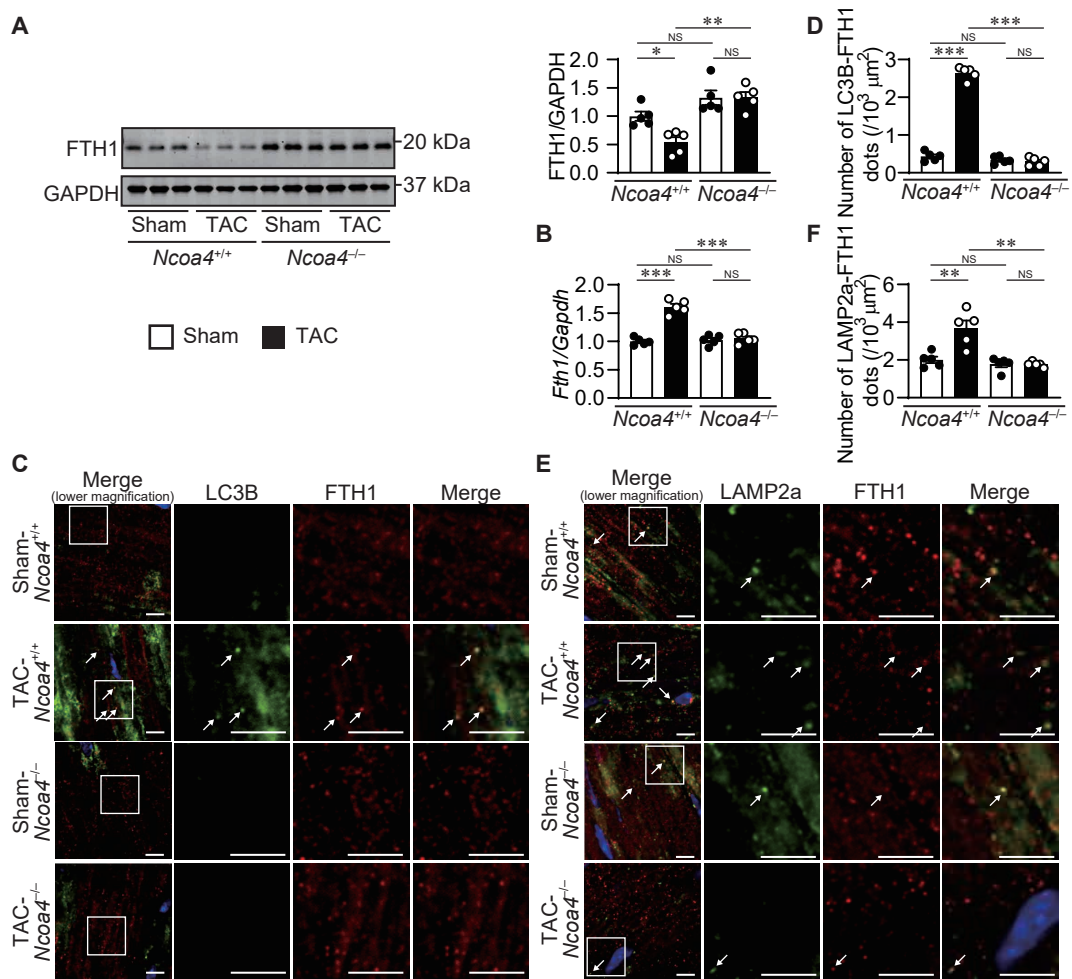
Figure 3

Figure 4

Figure 5

Figure 6

**Figure 1—figure supplement 1. Generation of cardiomyocyte-specific NCOA4-deficient mice**. (**A**) Targeted modification of the *Ncoa4* gene. Schematic structures of the wild-type genomic *Ncoa4* sequence, the targeting construct, the targeted allele, the floxed allele after flippase recognition target site (*FRT*)-mediated *neomycin*-resistance gene (*Neo*) deletion, and the deleted allele after Cre-mediated recombination are indicated from *top* to *bottom*. The *black* and *white arrowheads* indicate *loxP* and *FRT* sites, respectively. The *neomycin* resistance gene (*PGK-Neo* cassette) was inserted between exon 6 and the downstream *loxP* site. The diphtheria toxin A (*DT*) gene was positioned at the 3' end of the targeting construct for negative selection. The *bar* labelled as "probe" corresponds to the sequence used for Southern blotting. The scale bar indicates 2 kbp. (**B**) Genomic analysis of embryonic stem (ES) cells. To identify homologous recombinants, genomic DNA extracted from ES cells was digested with EcoRV and analyzed by Southern blotting with the 5' and 3' probe, respectively. Wild-type and targeted allele respectively showed 7,748 and 6,172 bp using the 5' probe (left) and 5,269 and 6,924 bp using the 3' probe (right). The ES cells with *Ncoa4*-floxed allele were injected into blastocysts to obtain *Ncoa4*<sup>flox/+</sup> mice. (**C**) Protein expression levels of NCOA4 in *Ncoa4*<sup>+/+</sup> and *Ncoa4*<sup>−/−</sup> hearts. Left ventricular homogenates from *Ncoa4*<sup>+/+</sup> and *Ncoa4*<sup>−/−</sup> mice were immunoprecipitated with anti-NCOA4 antibody, followed by Western blotting with the antibody. Densitometric analysis is shown. (**D**) mRNA expression levels of *Ncoa4*. The average value of NCOA4 (C) or *Ncoa4*-to-*Gapdh* ratio (D) in *Ncoa4*<sup>+/+</sup> was set equal to 1. The values are presented as the mean ± SEM of 4 mice for protein expression and 8 mice for mRNA expression in each group. The data were evaluated by unpaired, two-tailed Student's *t*-test. Source Data file is provided for Figure 1—figure supplement 1C and D.

**Figure 1—figure supplement 2. Physiological and echocardiographic parameters in 8- to 10-week-old *Ncoa4*<sup>+/+</sup> and *Ncoa4*<sup>–/–</sup> mice at baseline.**

| | *Ncoa4*$^{+/+}$ ($n$ = 8) | | | *Ncoa4*$^{-/-}$ ($n$ = 8) | | | *P* value |
|---|---|---|---|---|---|---|---|
| Body weight (g) | 25.7 | ± | 0.5 | 25.7 | ± | 0.4 | 0.925 |
| Tibia length (mm) | 16.8 | ± | 0.1 | 16.8 | ± | 0.2 | 0.854 |
| Systolic BP (mmHg) | 103 | ± | 2 | 100 | ± | 3 | 0.350 |
| Heart rate (bpm) | 709 | ± | 2 | 712 | ± | 2 | 0.368 |
| Heart weight/TL (mg/mm) | 8.20 | ± | 0.34 | 8.18 | ± | 0.18 | 0.955 |
| LV weight/TL (mg/mm) | 5.71 | ± | 0.27 | 5.79 | ± | 0.13 | 0.792 |
| Lung weight/TL (mg/mm) | 8.94 | ± | 0.23 | 9.06 | ± | 0.21 | 0.700 |
| LVIDd (mm) | 3.13 | ± | 0.04 | 3.08 | ± | 0.04 | 0.360 |
| LVIDs (mm) | 1.55 | ± | 0.03 | 1.52 | ± | 0.02 | 0.384 |
| IVSd (mm) | 0.74 | ± | 0.01 | 0.75 | ± | 0.004 | 0.055 |
| LVPWd (mm) | 0.73 | ± | 0.01 | 0.73 | ± | 0.003 | 0.221 |
| FS (%) | 50.7 | ± | 0.4 | 50.7 | ± | 0.4 | 0.909 |

BP, blood pressure; TL, tibia length; LV, left ventricle; LVIDd, end-diastolic left ventricular internal dimension; LVIDs, end-systolic left ventricular internal dimension; IVSd, end-diastolic interventricular septum thickness; LVPWd, end-diastolic left ventricular posterior wall thickness; FS, fractional shortening. The data are the mean ± SEM. *n* indicates the number of biologically independent samples. The data were evaluated by unpaired, two-tailed Student's *t*-test. Source Data file is provided for Figure 1—figure supplement 2.
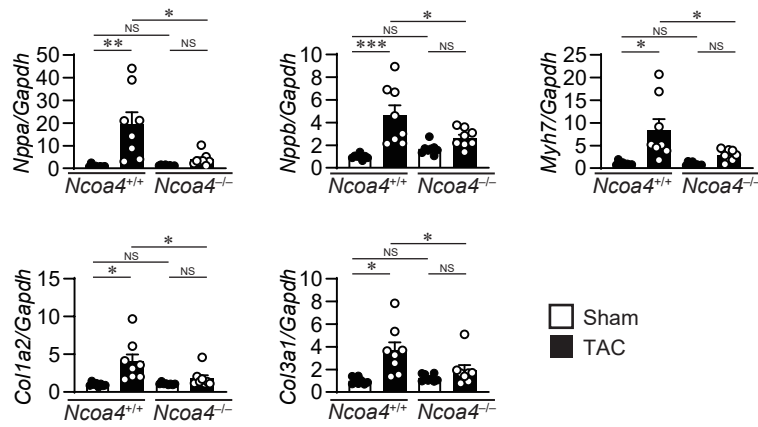
**Figure 1—figure supplement 3. Cardiac remodeling markers in TAC-operated _Ncoa4_$^{-/-}$ mice**. The _Ncoa4_$^{+/+}$ and _Ncoa4_$^{-/-}$ mice were subjected to TAC. The levels of mRNA were analyzed 4 weeks after the operation (_n_ = 8 biologically independent samples). _Gapdh_ mRNA was used as the loading control. The values are presented as the mean ± SEM. The data were evaluated by one-way analysis of variance (ANOVA), followed by Tukey–Kramer's post hoc test. *_P_ < 0.05, **_P_ < 0.001, ***_P_ < 0.0001. NS, _P_ > 0.05. Exact _P_ values are provided in Supplementary file 1. Source Data file is provided for Figure 1—figure supplement 3.
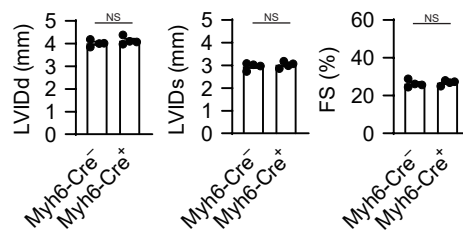
**Figure 1—figure supplement 4. Myh6-Cre transgene does not alter the heart response to pressure overload stress**. The Myh6-Cre⁻ and Myh6-Cre⁺ mice were subjected to TAC and analyzed 4 weeks after the operation. Echocardiographic parameters of the mice ($n = 4$ biologically independent samples) are shown. LVIDd and LVIDs, end-diastolic and end-systolic left ventricular (LV) internal dimensions; FS, fractional shortening. The values are presented as the mean ± SEM. The data were evaluated by unpaired, two-tailed Student's $t$-test. NS, $P > 0.05$. Exact $P$ values are provided in Supplementary file 1. Source Data file is provided for Figure 1—figure supplement 4.
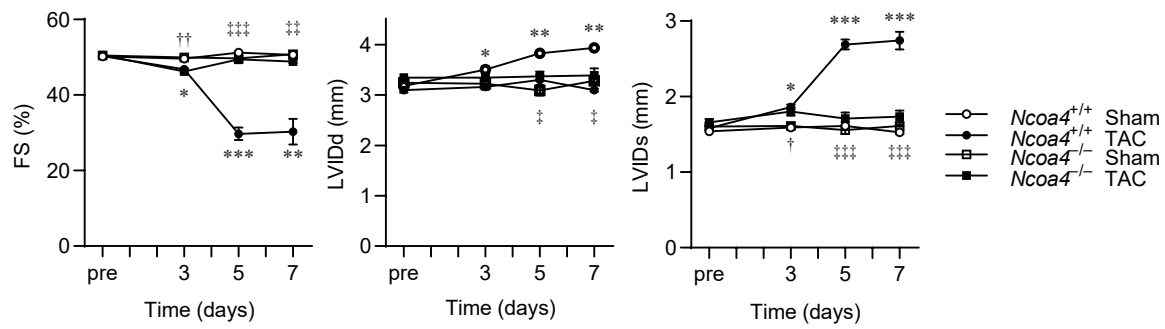
**Figure 2—figure supplement 1. Echocardiographic parameter after TAC.** Time course of changes in the echocardiographic parameters of left ventricular (LV) fractional shortening (FS) the end-diastolic LV internal dimension (LVIDd) and the end-systolic LV internal dimension (LVIDs). Echocardiographic analysis on *Ncoa4$^{+/+}$* and *Ncoa4$^{-/-}$* mice were performed before (pre) and 3, 5, and 7 days after TAC (n = 3 biologically independent samples). The values are presented as the mean ± SEM. Two-way analysis of variance (ANOVA) followed by Tukey's multiple comparisons test was used. *$P < 0.05$, **$P < 0.001$, ***$P < 0.0001$.    $P > 0.05$, sham-operated *Ncoa4$^{+/+}$* versus TAC-operated *Ncoa4$^{+/+}$*. †$P < 0.05$, ††$P < 0.001$, †††$P < 0.0001$. $P > 0.05$, sham-operated *Ncoa4$^{-/-}$* versus TAC-operated *Ncoa4$^{-/-}$*. ‡$P < 0.05$, ‡‡$P < 0.001$, ‡‡‡$P < 0.0001$. $P > 0.05$, TAC-operated *Ncoa4$^{+/+}$* versus TAC-operated *Ncoa4$^{-/-}$*. Exact $P$ values are provided in Supplementary file 1. Source Data file is provided for Figure 2—figure supplement 1.

**Figure 4—figure supplement 1. Hematological parameters and red cell indices in *Ncoa4*^{+/+} and *Ncoa4*^{−/−} mice**.

| | *Ncoa4*^{+/+} | | | | *Ncoa4*^{−/−} | | | |
|---|---|---|---|---|---|---|---|---|
| | Sham (*n* = 6) | | TAC (*n* = 6) | | Sham (*n* = 6) | | TAC (*n* = 6) | |
| Hemoglobin (g/dl) | 13.4 | ± 0.2 | 13 | ± 0.3 | 13.3 | ± 0.1 | 12.9 | ± 0.3 |
| PCV (%) | 43.2 | ± 1.3 | 41.8 | ± 1.1 | 42.3 | ± 0.9 | 41.4 | ± 1.2 |
| MCV (%) | 47.7 | ± 1.5 | 48.5 | ± 0.7 | 47.9 | ± 1.4 | 48.6 | ± 1.2 |
| MCH (pg) | 14.8 | ± 0.1 | 14.9 | ± 0.1 | 15.1 | ± 0.1 | 15.1 | ± 0.1 |
| MCHC (g/dl) | 31.2 | ± 0.8 | 30.7 | ± 0.3 | 31.7 | ± 0.7 | 31.1 | ± 0.7 |
| CH (pg) | 12.1 | ± 0.3 | 11.1 | ± 0.4 | 11.8 | ± 0.2 | 11.0 | ± 0.6 |
| Reticulocytes ($10^3/\mu l$) | 303 | ± 11 | 282 | ± 23 | 328 | ± 15 | 312 | ± 26 |
| Red cell count ($10^{12}$/l) | 9.02 | ± 0.12 | 8.63 | ± 0.14 | 8.83 | ± 0.11 | 8.52 | ± 0.25 |
| | Sham (*n* = 8) | | TAC (*n* = 8) | | Sham (*n* = 8) | | TAC (*n* = 8) | |
| Serum ferritin (ng/dl) | 86 | ± 6 | 50 | ± 5[*] | 106 | ± 15 | 63 | ± 7[**] |
| Serum iron (mg/dl) | 138 | ± 5 | 129 | ± 9 | 151 | ± 11 | 162 | ± 18 |
| Transferrin saturation (%) | 50.3 | ± 1.8 | 40.8 | ± 1.9 | 45.7 | ± 2.4 | 44.3 | ± 3.9 |

PCV, packed cell volume; MCV, mean corpuscular volume; MCH, mean corpuscular hemoglobin; MCHC, mean corpuscular hemoglobin concentration; CH, hemoglobin concentration. Data are the mean ± SEM. *n* indicates the number of biologically independent samples. The data were evaluated by one-way analysis of variance (ANOVA), followed by Tukey–Kramer's post hoc test. [*]$P$ = 0.0418 and [**]$P$ = 0.0108 versus the corresponding sham-operated group. Exact $P$ values are provided in Supplementary file 1. Source Data file is provided for Figure 4—figure supplement 1.
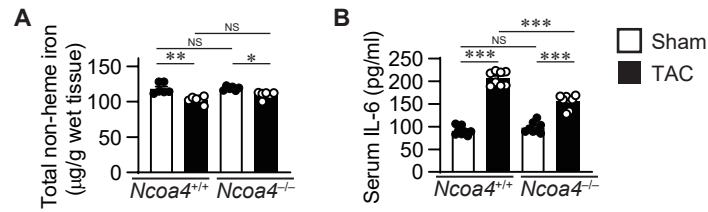
**Figure 4—figure supplement 2. Liver iron store and serum inflammatory cytokine in** *Ncoa4*^{+/+} **and** *Ncoa4*^{-/-} **mice**. (**A**) Tissue levels of total non-heme iron in *Ncoa4*^{+/+} and *Ncoa4*^{-/-} livers 4 weeks after TAC (n = 6 biologically independent samples). (**B**) Serum interleukin 6 (IL-6) levels (*n* = 8 biologically independent samples). The values are presented as the mean ± SEM. The data were evaluated by one-way analysis of variance (ANOVA), followed by Tukey–Kramer's post hoc test. $^*P < 0.05$, $^{**}P < 0.001$, $^{***}P < 0.0001$. NS, $P > 0.05$. Exact $P$ values are provided in Supplementary file 1. Source Data file is provided for Figure 4—figure supplement 2A and B.
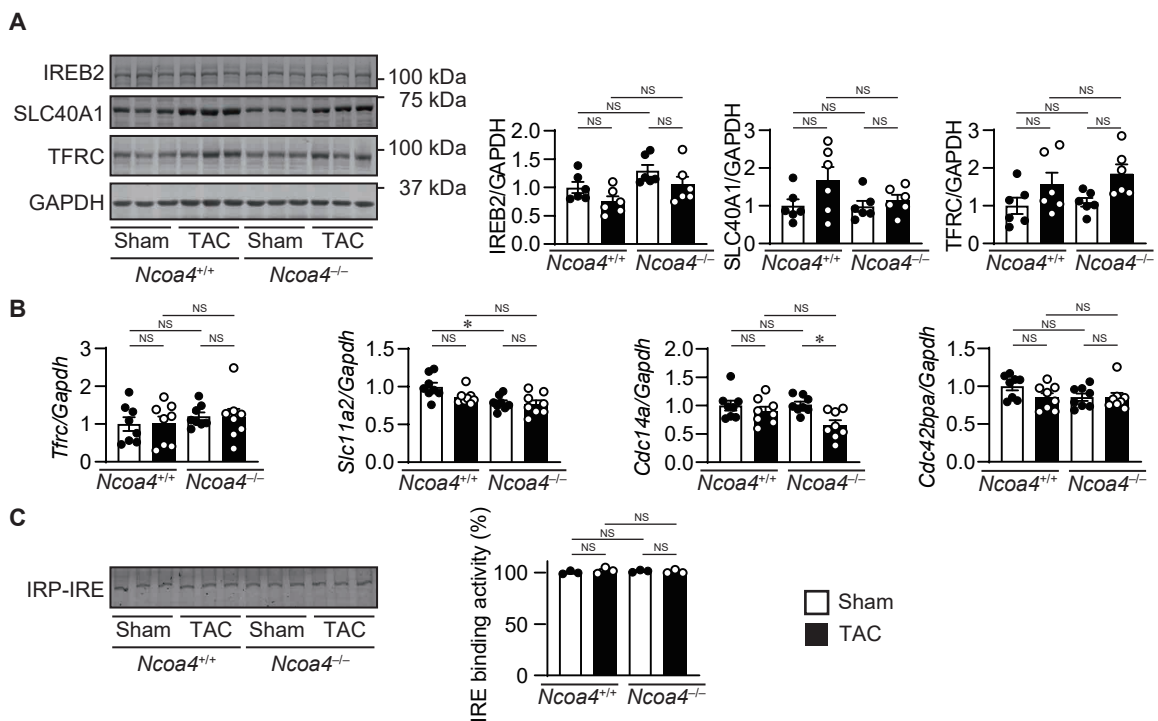
**Figure 4—figure supplement 3. Iron regulating proteins in TAC-operated *Ncoa4*<sup>–/–</sup> hearts**. (**A**) Homogenates from the heart 4 weeks after TAC were subjected to Western blot analysis using antibodies against iron-responsive element-binding protein 2 (IREB2), ferroportin 1 (SLC40A1), and transferrin receptor 1 (TFRC) (*n* = 6 biologically independent samples). GAPDH was used as the loading control. (**B**) The levels of mRNA were analyzed 4 weeks after the operation (*n* = 8 biologically independent samples). *Gapdh* mRNA was used as the loading control. (**C**) IRP activation in *Ncoa4*<sup>+/+</sup> and *Ncoa4*<sup>–/–</sup> hearts. The activation of IRP was analyzed by EMSA. Protein homogenates from mouse heart were incubated with the 5' UTR of mouse *Slc40a1* containing IRE and subjected to electrophoresis. (*n* = 3 biologically independent samples). The values are presented as the mean ± SEM. The data were evaluated by one-way analysis of variance (ANOVA), followed by Tukey–Kramer's post hoc test. NS, $P > 0.05$. Exact *P* values are provided in Supplementary file 1. Source Data file is provided for Figure 4—figure supplement 3A, B, and C.
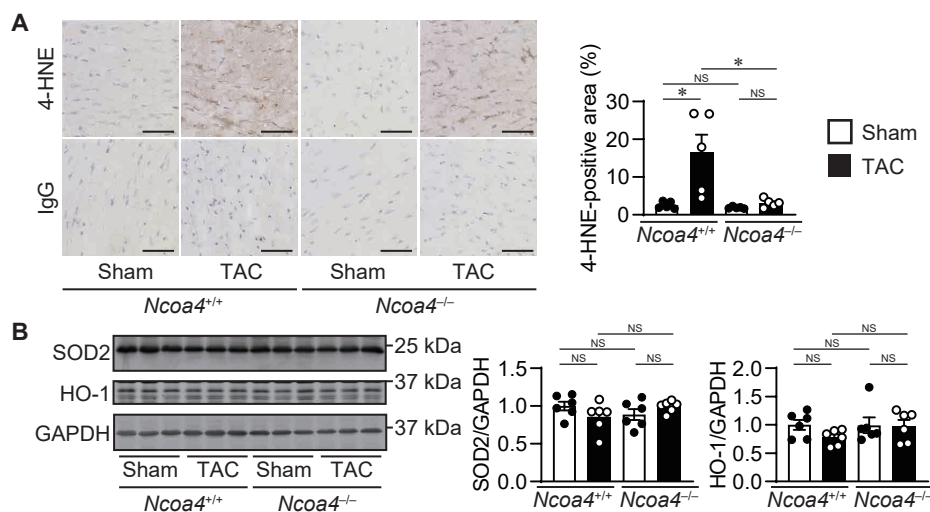
**Figure 4—figure supplement 4. Lipid reactive oxygen species and anti-oxidant proteins in *Ncoa4*$^{-/-}$ hearts four weeks after TAC**. (**A**) 4-Hydroxy-2-noneal (HNE) staining of heart sections. Scale bar, 50 μm. The right panel shows the quantitative analysis of 4-HNE-positive area to whole heart section (*n* = 5 biologically independent samples). (**B**) Homogenates from the heart were subjected to Western blot analysis using antibodies against superoxide dismutase 2 (SOD2) and heme oxygenase 1 (HO-1) (*n* = 6 biologically independent samples). GAPDH was used as the loading control. The values are presented as the mean ± SEM. The data were evaluated by one-way analysis of variance (ANOVA), followed by Tukey–Kramer's post hoc test. *$P < 0.05$. NS, $P > 0.05$. Exact *P* values are provided in Supplementary file 1. Source Data file is provided for Figure 4—figure supplement 4A and B.
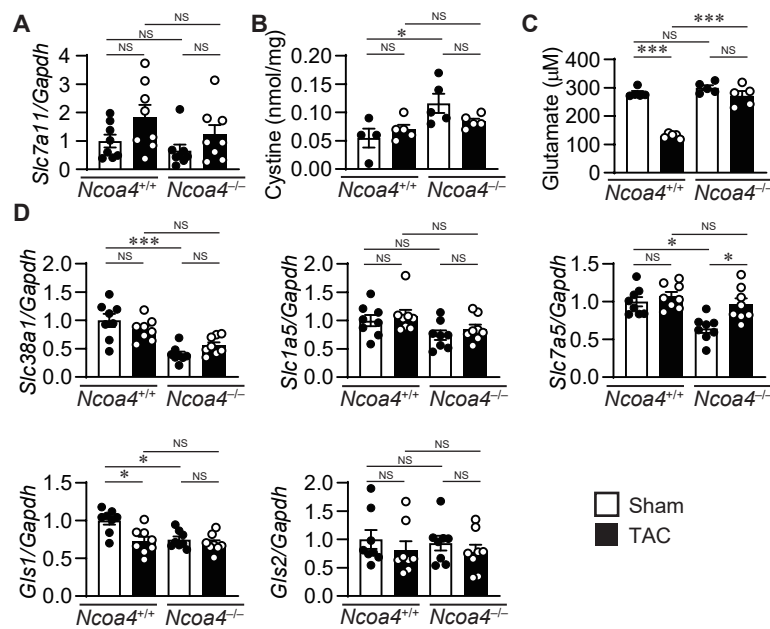
**Figure 4—figure supplement 5. The system Xc⁻/glutathione axis and glutaminolysis pathway in TAC-operated *Ncoa4⁻/⁻* hearts**. (**A**) The mRNA expression level of *Slc7a11* in the heart 4 weeks after TAC ($n = 8$ biologically independent samples). *Gapdh* mRNA was used as the loading control. (**B**) The cystine concentration in the heart was analyzed by high–performance liquid chromatography (HPLC) ($n = 4$ for sham-operated *Ncoa4⁺/⁺*, $n = 5$ for TAC-operated *Ncoa4⁺/⁺*, sham-operated *Ncoa4⁻/⁻*, and TAC-operated *Ncoa4⁻/⁻* biologically independent samples). (**C**) Cardiac glutamate levels ($n = 5$ biologically independent samples). (**D**) The mRNA expression levels of *Slc38a1*, *Slc1a5*, *Slc7a5*, *Gls1,* and *Gls2* in the hearts 4 weeks after TAC ($n = 8$ biologically independent samples). *Gapdh* mRNA was used as the loading control. The values are presented as the mean ± SEM. The data were evaluated by one-way analysis of variance (ANOVA), followed by Tukey–Kramer's post hoc test. *$P < 0.05$, ***$P < 0.0001$. NS, $P > 0.05$. Exact $P$ values are provided in Supplementary file 1. Source Data file is provided for Figure 4—figure supplement 5A, B, C, and D.
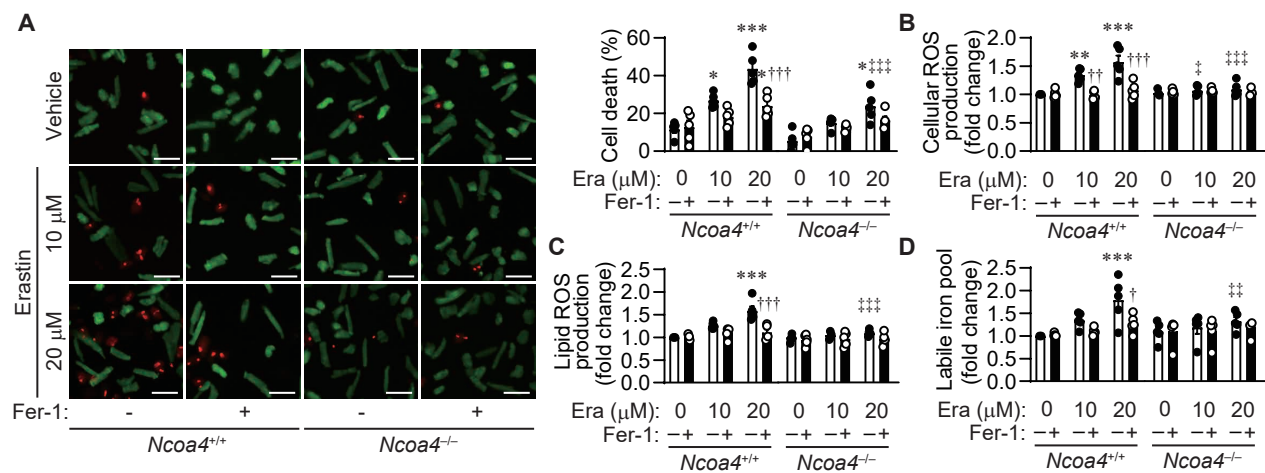
**Figure 5—figure supplement 1. Erastin induces cell death in isolated cardiomyocytes.** (**A**) Cell death assay. Cell death was estimated using a Live/Dead Viability/Cytotoxicity Assay Kit. Isolated mouse cardiomyocytes from *Ncoa4*$^{+/+}$ and *Ncoa4*$^{-/-}$ hearts were treated with the indicated concentrations of erastin (Era) with or without ferrostatin-1 (Fer-1) for 4 hours. Calcein-AM (green) is retained in live cells, while ethidium homodimer produces red fluorescence in dead cells. Scale bar, 100 μm. The percentage of dead cells is shown in the middle left-hand graphs ($n$ = 5 biologically independent samples). (**B and C**) The accumulation of cellular (B) and lipid (C) reactive oxygen species (ROS) were assessed by H2DCFDA and C11-BODIPY, respectively ($n$ = 5 biologically independent samples). (**D**) The labile iron pool was measured using the calcein-AM method in isolated mouse cardiomyocytes ($n$ = 5 biologically independent samples). The average value for vehicle-treated without ferrostatin-1 *Ncoa4*$^{+/+}$ cardiomyocytes was set to 1. The values are presented as the mean ± SEM. Two-way analysis of variance (ANOVA) followed by Tukey's multiple comparisons test was used. $^{*}P$ < 0.05, $^{**}P$ < 0.001, $^{***}P$ < 0.0001. NS, $P$ > 0.05 versus *Ncoa4*$^{+/+}$ control without ferrostatin-1 treatment. $^{†}P$ < 0.05, $^{††}P$ < 0.001, $^{†††}P$ < 0.0001. NS, $P$ > 0.05 versus the corresponding group without ferrostatin-1 treatment. $^{‡}P$ < 0.05, $^{‡‡}P$ < 0.001, $^{‡‡‡}P$ < 0.0001. NS, $P$ > 0.05 versus the corresponding *Ncoa4*$^{+/+}$. Exact $P$ values are provided in Supplementary file 1. Source Data file is provided for Figure 5—figure supplement 1A, B, C, and D.
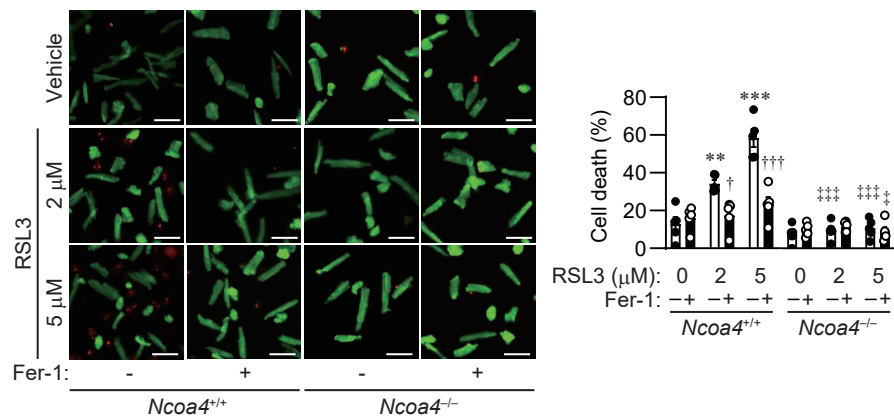
**Figure 5—figure supplement 2. RSL3 induces cell death in isolated cardiomyocytes**. Cell death assay. Cell death was estimated using a Live/Dead Viability/Cytotoxicity Assay Kit. Isolated mouse cardiomyocytes from $Ncoa4^{+/+}$ and $Ncoa4^{-/-}$ hearts were treated with the indicated concentrations of RSL3 with or without ferrostatin-1 (Fer-1) for 4 hours. Calcein-AM (green) is retained in live cells, while ethidium homodimer produces red fluorescence in dead cells. Scale bar, 100 μm. The percentage of dead cells is shown in the graphs ($n = 5$ biologically independent samples). The values are presented as the mean ± SEM. Two-way analysis of variance (ANOVA) followed by Tukey's multiple comparisons test was used. *$P < 0.05$, **$P < 0.001$, ***$P < 0.0001$. NS, $P > 0.05$ versus $Ncoa4^{+/+}$ control without ferrostatin-1 treatment. †$P < 0.05$, ††$P < 0.001$, †††$P < 0.0001$. NS, $P > 0.05$ versus the corresponding group without ferrostatin-1 treatment. ‡$P < 0.05$, ‡‡$P < 0.001$, ‡‡‡$P < 0.0001$. NS, $P > 0.05$ versus the corresponding $Ncoa4^{+/+}$. Exact $P$ values are provided in Supplementary file 1. Source Data file is provided for Figure 5—figure supplement 2.
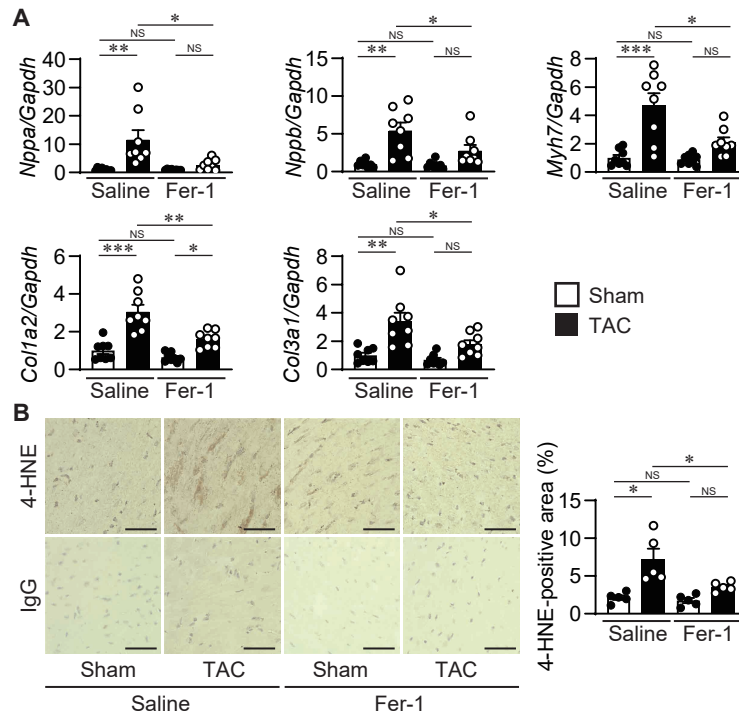
**Figure 6—figure supplement 1**. **Cardiac remodeling markers and 4-HNE staining in ferrostatin-1-treated TAC-operated wild-type hearts**. The wild-type C57BL/6J mice were subjected to TAC. Ferrostatin-1 (Fer-1) was intraperitoneally administered daily starting one day before TAC. (**A**) The levels of mRNA were analyzed 4 weeks after the operation ($n = 8$ biologically independent samples). *Gapdh* mRNA was used as the loading control. (**B**) 4-Hydroxy-2-noneal (4-HNE) staining of heart sections. Scale bar, 50 µm. The right panel shows the quantitative analysis of 4-HNE-positive area ($n = 5$ biologically independent samples). The values are presented as the mean ± SEM. The data were evaluated by one-way analysis of variance (ANOVA) followed by Tukey–Kramer's post hoc test. $^*P < 0.05$, $^{**}P < 0.001$, $^{***}P < 0.0001$. NS, $P > 0.05$. Exact $P$ values are provided in Supplementary file 1. Source Data file is provided for Figure 6—figure supplement 1A and B.
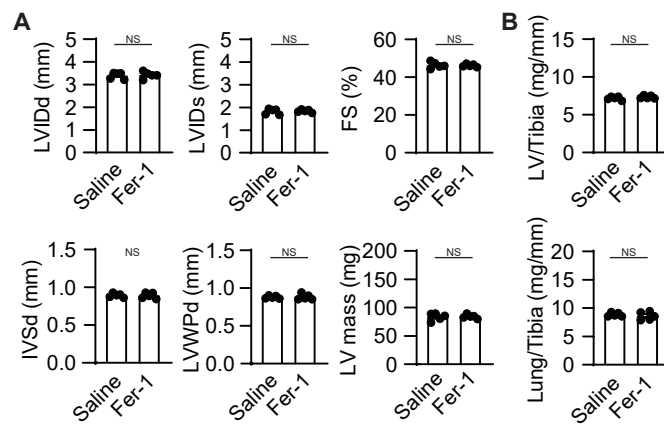
**Figure 6—figure supplement 2**. **Ferrostatin-1 does not provide additional protection from cardiac remodeling in *Ncoa4⁻/⁻* mice**. The *Ncoa4⁻/⁻* mice were subjected to TAC. Ferrostatin-1 (Fer-1) or saline was intraperitoneally administered daily starting one day before TAC. (**A**) Echocardiographic parameters of the mice (*n* = 5 biologically independent samples). LVIDd and LVIDs, end-diastolic and end-systolic left ventricular (LV) internal dimensions; IVSd, end-diastolic interventricular septum thickness; LVPWd, end-diastolic LV posterior wall thickness; FS, fractional shortening. (**B**) Physiological parameters of the mice (*n* = 5 biologically independent samples). The values are presented as the mean ± SEM. The data were evaluated by unpaired, two-tailed Student's *t*-test. NS, $P > 0.05$. Exact *P* values are provided in Supplementary file 1. Source Data file is provided for Figure 6—figure supplement 2A and B.